Measuring Phase Modulation with Scanning Differential Heterodyne Microscopy

MSc Thesis

Cian Dooley

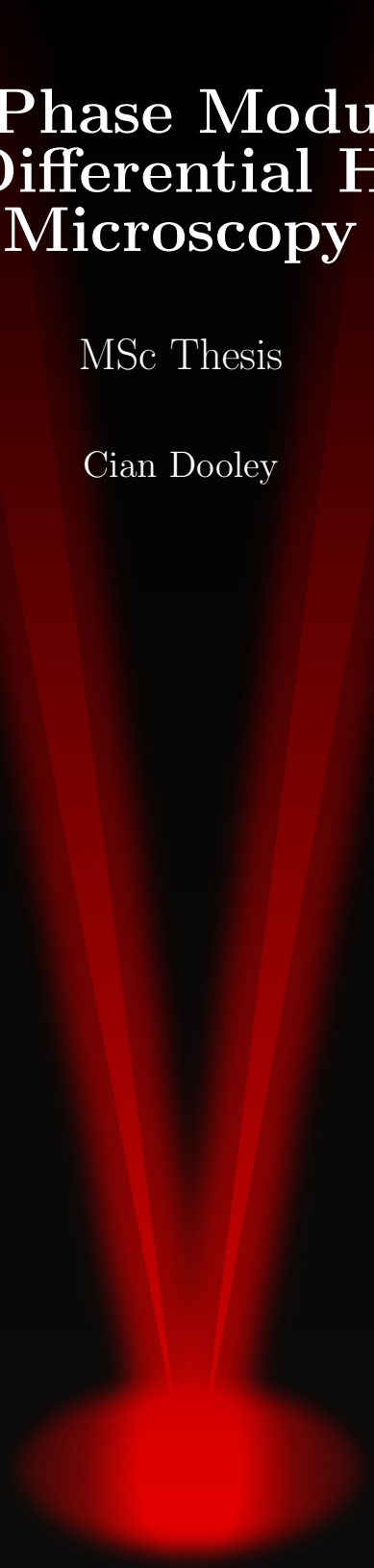

UNIVERSITY OF AMSTERDAM

VRIJE UNIVERSITEIT AMSTERDAM

Institute of Physics
University of Amsterdam
18th July 2025

Daily Supervisors: Bernardo S. Dias MSc, Tom Hoekstra MSc
Supervisor: Dr. Jorik van de Groep
Examiner: Prof. dr. Mark S. Golden

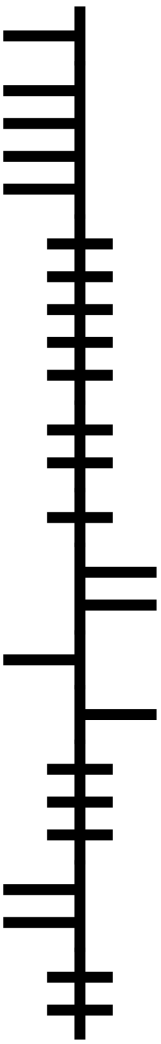

Tada Gan Iarracht

Abstract

The manipulation of light is used in a wide variety of devices today, made possible by the invention of the optical lens. Simply by manipulating light with lenses, devices such as cameras, microscopes, augmented reality glasses, and LiDAR have been developed. While these devices are constantly evolving, the improvement in optical components cannot keep up with the decreasing transistor size in electrical components due to a crucial limitation: the size of a lens cannot be reduced without decreasing its functionality. This unfortunate limitation results in compact electrical devices using bulky optical components that stick out of the device, like a camera on the newest generations of phones. A solution to this problem involves using metasurfaces, 2D materials with nano-structures on the surface, which can be designed to behave like a lens while being much thinner. These surfaces alone can already improve the standard of optical devices. However, since each surface is fixed, its design can only fulfill a single task. By incorporating modulation into these metasurfaces (by including materials that change their optical properties due to an applied gating voltage), the functionality of each design can be increased, further improving the devices currently using bulky optical components.

To effectively design and build such metasurfaces and measure the effect of the surface on light, the phase of the light must be detectable for the entire phase range ($0 \rightarrow 2\pi$ radians) and in as small an increment as possible. This is challenging for light in the visible spectrum because photo-detectors are not fast enough to measure the oscillations of the light's electric field, meaning the phase information of the light is lost when it is incident on a photo-detector. To sidestep this issue, a technique known as heterodyne detection is harnessed to measure the phase of a visible laser source. Implementing this technique, the laser is reflected from various samples to validate the simulations with experiments before finally measuring the change in phase while modulating the optical properties of a TMD with a gating voltage. Future work should highlight the extent to which this technique can measure small phase changes and expand upon the research by testing various samples during modulation.

This project reports the results from measurements of an active 2D material designed to modulate the phase of light as it is reflected from the surface. A detailed analysis of the heterodyne system is provided, including the experimental setup and the model used for simulations.

Contents

1 Introduction

Manipulating light with the invention of the first lens paved the way for advancement in optical devices [1]. Lenses in spectacles, cameras, and microscopes are some examples of the wide variety of uses optical manipulation has in our everyday lives. As these devices become more advanced and perform more functions, they require an increasing number of components to accomplish all these different tasks. Historically, as optical setups perform more complex functions, the size of these setups tends to increase, mostly due to the need to respect phase accumulation effects from free space propagation. Unlike electronic components, which have realized continuously reduced device dimensions by shrinking the transistors, optical components do not follow the same trend.

For example, unlike electrical components, optical components like a lens cannot easily be made smaller without losing a lot of the light and thus reducing the quality of the image. In order to capture enough light for a high-resolution image, the lenses in a camera must be wide. Since the thickness of the lenses increases with the overall size of the lens, larger lenses are thicker. A camera that produces high-quality images and performs multiple functions on these images must have a lot of these lenses stacked on top of each other; consequently, optical devices cannot shrink in size without sacrificing image quality or device functionality. Therefore, another method to capture enough light to maintain high-quality images while also reducing the size of the optical components is needed. The solution to this could be combining metasurfaces with 2D materials [2].

Metasurfaces are engineered 2D surfaces with sub-wavelength-sized nanoparticle structures designed to interact with light. These interactions can be controlled with the nanoparticle dimension and material [3]. These particles exhibit strong resonances at a particular wavelength, meaning the optical response from such a surface can be engineered with the nanoparticle design and orientation patterns across the surface [4]. Thus, the amplitude and phase responses from metasurfaces can be designed, which offers ultra-flat alternatives to optical devices. However, they are typically static.

2D materials are crystals that have strong in-plane molecular bonds, but each plane is only held together by weak van der Waals forces. When stripped down to very thin layers, these materials have interesting optical properties dominated by excitons within the material that offer a uniquely strong light-matter interaction that is tunable. This opens up the opportunity for active optical elements. Demonstrated examples include using atomically thin materials to perform light-focusing, optical modulation using electrical gating, and polarization control with graphene [5][6][7]. The versatility of 2D materials is also evident with the implementation of multifunctional tools, such as simultanious optical modulation and photodetection, and modulation and plasmon waveguides [8][9][10]. The excitons in 2D materials are capable of being quenched when a gating voltage is applied across the material. This causes the optical properties to be changed when switching between “On” (no voltage) and “Off” (electrical gating) [11]. By combining the strong excitonic properties of 2D materials with the modulation during electrical gating, it could be possible to achieve a phase modulated structure that operates at visible wavelengths to replace the bulky lenses currently used in optical devices like cameras.

To explore tunable 2D metasurfaces, we need to be able to electrically control the scattered amplitude and phase. While measuring amplitudes is facile, measuring phase is more challenging. Most optical devices that we use operate in the visible spectrum, and unfortunately, the frequency of visible light is too high for standard photo-detectors to detect. This means that the oscillations of visible light are averaged to a DC signal when incident on a photo-detector, and as a result, the phase information of the light is lost. Since the phase is a quantity we would like to measure for modulated devices, it is essential to find a method of measuring this for visible wavelengths.

Two common techniques for the direct measurement of the phase of light are homodyne detection and heterodyne detection [12] [13]. Both methods involve mixing a signal with a local oscillator (LO) as a reference to extract amplitude and phase information. Homodyne detection uses a LO with the same frequency as the signal and extracts the phase from the change in amplitude of the interference signal (intensity is maximum when in phase and minimum with a π phase difference) [12]. However, heterodyne detection is a process that involves interfering two beams of different frequency light, resulting in an oscillating beat signal that changes in phase depending on the change in phase difference between the signal and the LO. The phase of this beating signal can be detected as long as the signal frequency is within the range for the photo-detector to resolve. Therefore, the interference signal can be used to probe tunable structures and determine the phase and amplitude change in the light as the material properties are modulated with a voltage.

In this thesis, we employ heterodyne detection integrated with a microscope to realize scanning differential heterodyne detection and use it to characterize phase and amplitude tuning in 2D heterostructure samples. First, we use the theory of the transfer matrix method to simulate the response from various samples and compare these simulations with experimental results. The design of the experimental setup and improvements made will also be discussed, leading to the final design and its specifications, which implement a technique known as scanning differential heterodyne microscopy. This technique measures the gradient of reflection phase across a surface, meaning the potential to map the phase across structures. Finally, the outlook will include further improvements that can be made to the setup to probe at different wavelengths or scan over smaller structures.

2 Scanning Differential Heterodyne Microscopy and Phase Modulation

In this chapter, the theory and implementation of scanning differential heterodyne microscopy (SDHM) are discussed. The design for the setup is presented, along with improvements to reduce noise that ultimately lead to the final setup, the configuration and stability of which are discussed in detail. Finally, the theory of phase modulation using the optical properties of 2D materials is explained.

2.1 Background

2.1.1 Heterodyne Detection - Beating Signal Equation

Heterodyne detection is the detection of the signal from two interfering laser beams with different frequencies. When two lasers of different frequencies f_1, f_2 (angular frequencies $\omega_1 = 2\pi f_1$, $\omega_2 = 2\pi f_2$) interfere, a beat signal is created. The frequency of this beating signal is equal to the difference in frequency of the individual waves. This can be shown by defining the electric fields for the LO and signal laser beams as $\mathbf{E_1}$ and $\mathbf{E_2}$ in Equation 2.1 [14].

$$\begin{aligned} \mathbf{E_1} &= Ae^{i\omega_1 t} + A^* e^{-i\omega_1 t} \\ \mathbf{E_2} &= Be^{i[\omega_2 t+\phi]} + B^* e^{-i(\omega_2 t+\phi)}, \end{aligned} \tag{2.1}$$

where A, B are the amplitudes of $\mathbf{E_1}, \mathbf{E_2}$. The definition of $\mathbf{E_2}$ in Equation 2.1 contains a phase term ϕ while $\mathbf{E_1}$ does not because in this technique the goal is to extract the phase $difference$ between the signal and LO beams. As such, $\mathbf{E_1}$ is defined as having phase $\phi_1 = 0$ and $\mathbf{E_2}$ is defined as having phase $\phi_2 = \phi$, where ϕ now acts as the difference in phase between the two beams.

Since a photo-detector measures the intensity $I_{\text{Detector}} \propto \mathbf{E}\mathbf{E}^*$ of a signal rather than the signal's electric field $\mathbf{E}$, the intensity of the interference between $\mathbf{E_1}$ and $\mathbf{E_2}$ is written as:

$$\begin{aligned} I_{\text{Detector}} &= \mathbf{E}_{\text{Sum}} \cdot \mathbf{E}^*_{\text{Sum}} = (\mathbf{E_1} + \mathbf{E_2}) \cdot (\mathbf{E_1^*} + \mathbf{E_2^*}) \\ &= \left(Ae^{i\omega_1 t} + A^* e^{-i\omega_1 t} + Be^{i[\omega_2 t+\phi]} + B^* e^{-i(\omega_2 t+\phi)}\right) \cdot \\ &\quad \left(A^* e^{-i\omega_1 t} + Ae^{i\omega_1 t} + B^* e^{-i[\omega_2 t+\phi]} + Be^{i(\omega_2 t+\phi)}\right) \\ &= A^2 + A^{*2} + B^2 + B^{*2} \\ &\quad + (AB + A^*B^*)\left(e^{i[(\omega_1-\omega_2)t-\phi]} + e^{-i[(\omega_1-\omega_2)t-\phi]}\right) \\ &\quad + (AB^* + A^*B)\left(e^{i[(\omega_1+\omega_2)t+\phi]} + e^{-i[(\omega_1+\omega_2)t+\phi]}\right) \\ &\quad + 2AA^*\cos(2\omega_1 t) + 2BB^*\cos(2\omega_2 t + 2\phi) \end{aligned} \tag{2.2}$$

The different components of Equation 2.2 are known as optical rectification (OR), difference-frequency generation (DFG), sum-frequency generation (SFG), and second-harmonic generation (SHG), respectively. Any frequencies other than $\omega_1 - \omega_2 = \Delta\omega$ are too high for standard photo-detectors to measure, and thus average to zero. Therefore, the higher frequency terms in Equation 2.2 (SFG, SHG) vanish, and the equation only includes the DC signals from the original waves (OR) and the interference term with $\Delta\omega$ (DFG), provided $\Delta\omega$ is within the detectable range of the photo-detector.

Since the detector only measures the real part $\Re$ of Equation 2.2, it becomes:

$$\begin{aligned} I_{\text{Detector}} &= \Re\left(A^2 + A^{*2} + B^2 + B^{*2} + (AB + A^*B^*)\left(e^{i[\Delta\omega t - \phi]} + e^{-i[\Delta\omega t - \phi]}\right)\right) \\ &= 2A^2 + 2B^2 + 2AB \cdot \Re\left(e^{i[\Delta\omega t - \phi]} + e^{-i[\Delta\omega t - \phi]}\right) \\ &= 2A^2 + 2B^2 + 4AB \cdot cos(\Delta\omega t - \phi) \end{aligned} \tag{2.3}$$

To extract the phase from this signal, the interference term containing the phase information can be isolated using a lock-in amplifier [15]. This is an instrument that takes a signal (in this case, the output from the photo-detector) and a reference (in this case a constant radio frequency signal at frequency $\Delta\omega$) and isolates the part of the signal at the reference frequency while ignoring all other frequencies in the signal. Using this tool, it is possible to separate the $\Delta\omega$ term in Equation 2.3 from the DC terms and all other frequency terms, leaving only the intensity of the beat signal I_{Beat} in Equation 2.4. By making $\Delta\omega$ small enough, a beating signal (red plot in Figure 2.1) is measurable on the detector with an oscillating intensity profile (black envelope).

$$I_{\text{Beat}} \propto AB \cdot cos(\Delta\omega t - \phi) \tag{2.4}$$

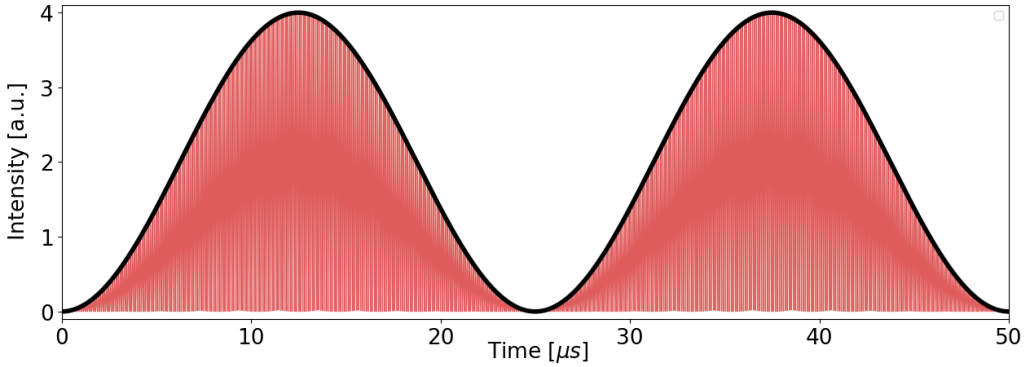

Figure 2.1: *Beating signal (red) formed when two waves of different frequencies interfere. The beating signal envelope frequency (black) is equal to the difference in frequency Δf. In this case, $\Delta f = 40$ kHz, where $f_1 = 473$ THz $= 4.73 \times 10^{11}$ kHz.*

2.1.2 Acousto-Optic Modulators - How to frequency shift light

An acousto-optic modulator (AOM) uses sound waves in a crystal to shift the frequency of incident light on the crystal [16]. An electrical radio-frequency (RF) signal is sent to a piezoelectric transducer, which converts the electrical signal into an acoustic wave that propagates through the crystal. This acoustic wave results in spatially periodic variations in the refractive index due to compression and expansion of the material in the direction of the acoustic wave through the crystal. The periodic refractive index acts as a moving diffraction grating that diffracts light as it passes through the crystal, as seen in Figure 2.2 [16][17].

If the incident light comes in under a specific angle, called the Bragg angle θ_B, the 0th-order beam (not frequency-shifted) travels in the same direction as the original incident light by exiting at an angle θ_B and the 1st-order diffracted beam exits the crystal at a different angle and frequency. By optimizing the incident angle, up to 90% of the light can be diffracted into the 1st-order. Depending on the direction of the incident light relative to the acoustic wave in the crystal, the 1st-order beam will be shifted up or down in frequency by an amount equal to the acoustic wave frequency. For example, the frequency of the 1st-order diffracted beam in Figure 2.2 increases. If the acoustic wave comes from the other direction, the frequency decreases. This frequency shift occurs due to the conservation of energy and momentum of the photons and phonons, where phonons are created or destroyed depending on the propagation direction of the acoustic wave relative to the incoming beam [18][16].

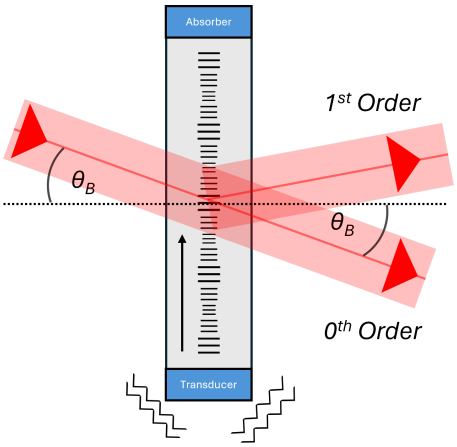

Figure 2.2: *Diffraction of light in an AOM when the incident light comes in under the Bragg angle. Due to the moving diffraction grating within the AOM crystal, the 1st-order diffracted beam has a higher intensity than the -1st-order beam, and is frequency-shifted with respect to the incoming beam.*

Therefore, the 1st-order beam can be shifted up or down in frequency by coming in at $\theta_{\text{In}} = \theta_{\text{B}}$ or $\theta_{\text{In}} = -\theta_{\text{B}}$. Another way of thinking this is by reversing the propagation direction of the acoustic wave in Figure 2.2.

In the setup in Figure 2.3, two AOMs are used to shift the frequency of the reference beam. The first AOM shifts the signal down by 200.02 MHz and the second AOM shifts the signal back up by 199.98 MHz, resulting in the reference beam being shifted by 40 kHz after passing through the AOM box. It is not possible to use a single AOM to shift the frequency by 40 kHz directly due to the operational bandwidth of the AOMs being in the 200 ± 1 MHz range and an AOM operating at 40 kHz would generate a moving diffraction grating with a spacing that's too large for the light to experience any diffraction.

The AOMs used in this setup are the MT200-A0.5-VIS model from AA Opto-Electronics [19]. Each AOM is connected to a phase-locked, multi-output, multi-channel DDS frequency synthesizer MPDS1C4X / MPDS2C4X [20][21] which generates the 200.02 MHz and 199.98 MHz RF signals, respectively.

2.2 Implementing Heterodyne Detection

2.2.1 Fiber Setup

The practical implementation of the heterodyne system uses two AOMs (described above) and a Melles Griot 05-LHP-121 632.8 nm HeNe laser [22]. The initial configuration for this laser has it coupled to a single-mode fused fiber-optic splitter (FS). This splits the coupled light 75:25 into two different paths.

The first path goes into a box where the laser is sent through the two AOMs to be frequency-shifted before re-coupling into a fiber-optic coupler. The AOMs change the frequency of the laser (as described in Section 2.1.2 by 40 kHz. The implementation of this box in Figure 2.3 has the frequency-shifted beams pass through the setup while the non-frequency-shifted beams are blocked using beam-blockers (BB). Both beams recombine in another fiber splitter before being incident on a photo-detector.
The second path from the laser (yellow fiber) is intended to be reflected off a sample.

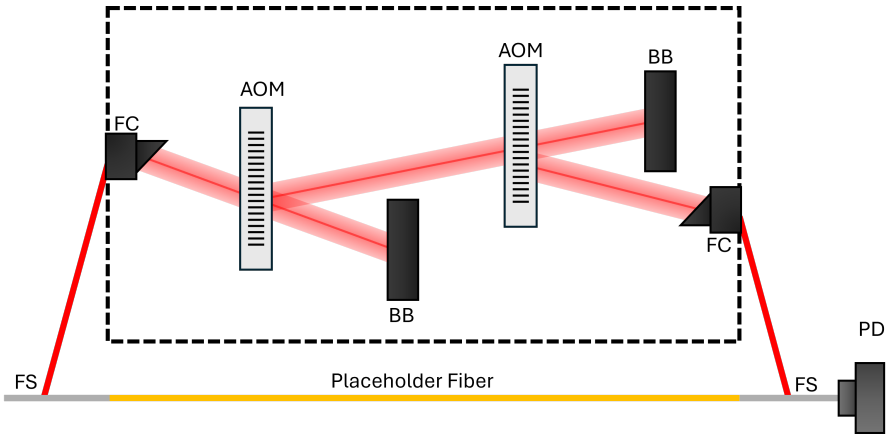

Figure 2.3: *Schematic for the fiber setup. The laser passes through a fiber splitter (FS), forming a frequency-shifted path (red, free space) and a sample-testing path (yellow, fiber). The frequency-shifted path uses AOMs, fiber-couplers (FC), and beam-blockers (BB) inside a box (black, dotted outline) before returning to a fiber to interfere with the sample-testing path. The yellow fiber being used is a placeholder intended to be interchanged with a material for testing.*

While the fibers in this design make it convenient, the stability of the phase is very low (see Figure 2.9 for a comparison) due to the fibers' sensitivity to thermal fluctuations in the air. The design can be improved by replacing some fibers with free space beam paths, as discussed next in Section 2.2.2.

2.2.2 Free Space Setup

Here, the fibers after the first fiber splitter are removed entirely to reduce the remaining phase drift. The path is the same for the laser beam that travels through the AOM box to be frequency-shifted. The main difference occurs in the beam intended to go to a material (yellow path in Figure 2.4). Here, the beams interfere in free space using mirrors and beamsplitters.

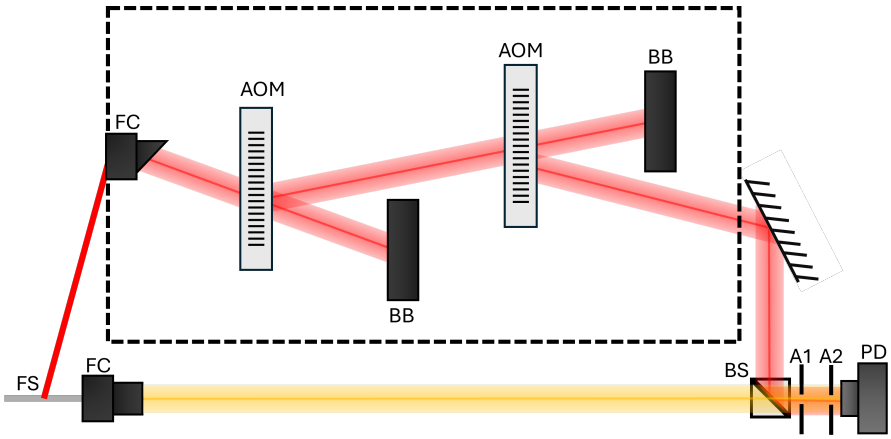

Figure 2.4: *Schematic of the setup, showing the differences made to the previous setup in Figure 2.3 to replace the fibers in Figure 2.3. As in the fiber setup, the non-frequency-shifted beam (yellow) is to be used for sample measurements.*

All-in-all, the phase in the free space setup is much more stable than in the fiber setup. As such, we will continue working in free space for the remainder of this thesis. However, while the stability is an improvement from the fiber setup, there is still too much noise to reliably measure a consistent phase shift. The final design uses a common path scheme to further eliminate any noise differences between both beam paths. This scheme is described in Section 2.2.3, which is the final design and is used for all subsequent experiments.

2.2.3 Common-Path Free Space Scheme

Even with the improvements described above, the noise in the free space setup prevents reliable phase measurements. As a result, the setup is updated to a Mach-Zehnder Interferometer, resembling the design found in literature [23]. The advantage this design has over the previous is that both beams share very similar paths, meaning any shifts in the temperature or vibrations in the mirrors are felt by both beams and so will reduce any large fluctuations that could occur.

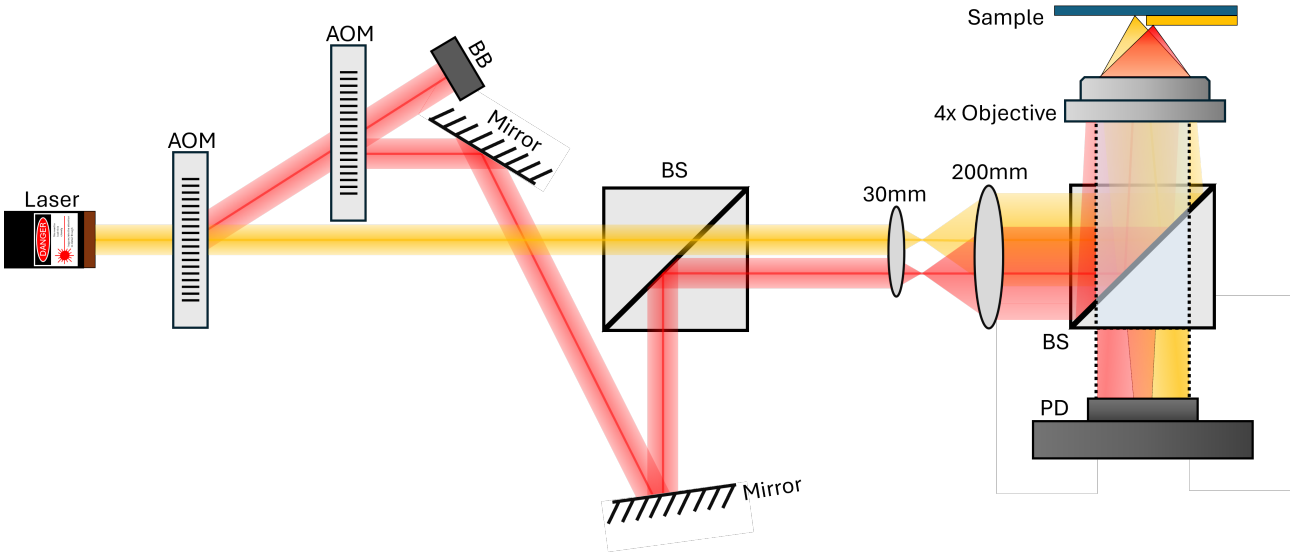

Figure 2.5: *Schematic of setup using common path scheme to further reduce noise in the phase measurements. The two incoming beams (red, yellow) and the reflected beam from the sample (white, dotted) are shown. This particular design uses a telescope system with 30 mm to 200 mm focal length lenses to expand the beams and a Nikon NA=0.13 objective to focus onto the sample [24]. There are two reflected beams (shown as white for clarity) which have an overlap (orange area before PD) in the Fourier plane at $k = 0$ (normal incidence).*

The method implemented in Figure 2.5 is called scanning differential heterodyne microscopy (SDHM), as there are two beams incident on the sample, and the difference between them now measures the local changes on the sample surface rather than the total change. The details on how this setup functions are discussed in Section 2.3, along with the stability and how the design is capable of measuring phase shifts. The design in Figure 2.5 is the setup design being used for all measurements discussed later.

2.3 Implementing SDHM

In this section, an explanation of the setup in Figure 2.5 is given, with an explanation on the role of each component and how it contributes to the level of stability seen in Section 2.3.2.

2.3.1 Experimental Setup

The laser source in this setup is the 633 nm HeNe CW laser [22]. After emission from the laser tube, the laser beam is directed into an AOM at the Bragg angle, resulting in a 0th-order beam and a 1st-order beam exiting from the AOM. One reason for the improvement of noise in this setup over previous setups is the application of both beams emitted from the first AOM, compared to the previous setups, which only make use of the 1st-order beams. This improves the phase stability as both beams experience the vibrations from the first AOM, reducing the difference in noise between the beams, similarly to why the phase stability is improved when both beams are incident on the sample optical components in Figure 2.5. In Equation 2.4, the ϕ term has less fluctuations and drift.

Upon transmission from the first AOM, the 0th-order beam is guided towards a beamsplitter. Meanwhile, the 1st-order beam is directed to the next AOM where it is frequency-shifted again before also being directed towards the same beamsplitter to re-combine with the 0th-order beam.

From here, both beams follow the same path towards the sample. There is a telescope system using two lenses (with focal lengths of 30 mm and 200 mm, respectively) to increase the beam sizes. After expansion, the beams are sent through another beamsplitter to be incident upon a Nikon CFI Plan Fluor Objective [24]. The beams are focused onto the sample surface and reflected to pass back through the beamsplitter, now guided towards an amplified photo-detector [25]. The signal from this photo-detector is connected to an SR830 DSP Lock-In Amplifier, which isolates the 40 kHz interference signal and extracts the amplitude and phase information [26][15].

The approach for measuring phase shifts involves both beams incident on the sample instead of just one beam, as seen in Figure 2.5. Here, the phase being measured is the $difference$ in phase between each beam, so the laser beams must be incident on different spots on the sample to ensure a phase difference is measured. The reason for this is described in detail in Section 3.2. In short, since the phase of the beating signal is dependent on the $difference$ in phase between each beam, a phase change is only detected when each beam experiences changes at different times. If the beams are incident on the same spot, they will experience a change at the same time, and nothing will be detected in the beating signal.

To achieve this, each beam is incident on the objective aperture at different angles [27][28]. This is evident in the schematic where each beam is colored differently in Figure 2.5. This ensures that the beam spots are separated on the sample, but the reflected light has enough overlap when incident on the photo-detector to detect a beating signal. This overlap occurs in Fourier space rather than in real space. Each beam is incident on the surface at a range of angles determined by the numerical aperture (NA) of the objective (high NA means a wider range of incidence angles, see Figure 2.6). This means the total response when a beam is scanned across the surface is the average response over all incident angles. To avoid measuring the response from non-normally incident light, the detector is placed at the back focal plane (BFP) of the objective, where the Fourier plane is imaged [29]. Using an aperture at the detector, all non-normal components of the reflected BFP image are blocked, so only the changes to normally incident light are observed. This can be seen in Figure 2.6, where the white ring shows the physical aperture placed in front of the detector to block all non-normally incident light (*i.e.* all light far away from the bright spot in the center of Fourier space, which represents the normally incident light). Figure 2.6 shows how this is achieved with two different NA objectives. For clarity, the Fourier plane is displayed as being the same size for both. In reality, the BFP would be different for different objective NAs [30][31]. For all results shown in this thesis (with NA = 0.13), the back focal lane is not imaged, but for higher NA the photo-detectoer should be positioned at the BFP of the objective.

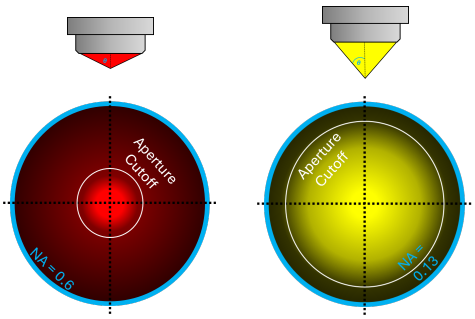

Figure 2.6: *Isolating normal components of reflected light using back focal plane (BFP) imaging.* ***(top)*** *An objective showing the difference in angular spread with high NA (red) and low NA (yellow). The BFP for each NA* ***(bottom)*** *is also shown in for high NA* ***(left)*** *and low NA* ***(right)****. The BFP images also display the aperture size to isolate the normal components of the reflected light.*

Alignment in free space requires manual beam adjustment to ensure enough overlap for a measurable beating signal. Otherwise, only a DC signal is detected, losing any phase information from the two laser beams. The technique used to improve the overlap takes advantage of the interference fringes that appear on a camera when the overlapping beams are of the same frequency. Better overlap between the beams leads to larger fringe spacing, as seen in Figure 2.7. The beams are set to the same

frequency by switching the RF AOM frequencies from 199.98 MHz and 200.02 MHz to both being 200.00 MHz.

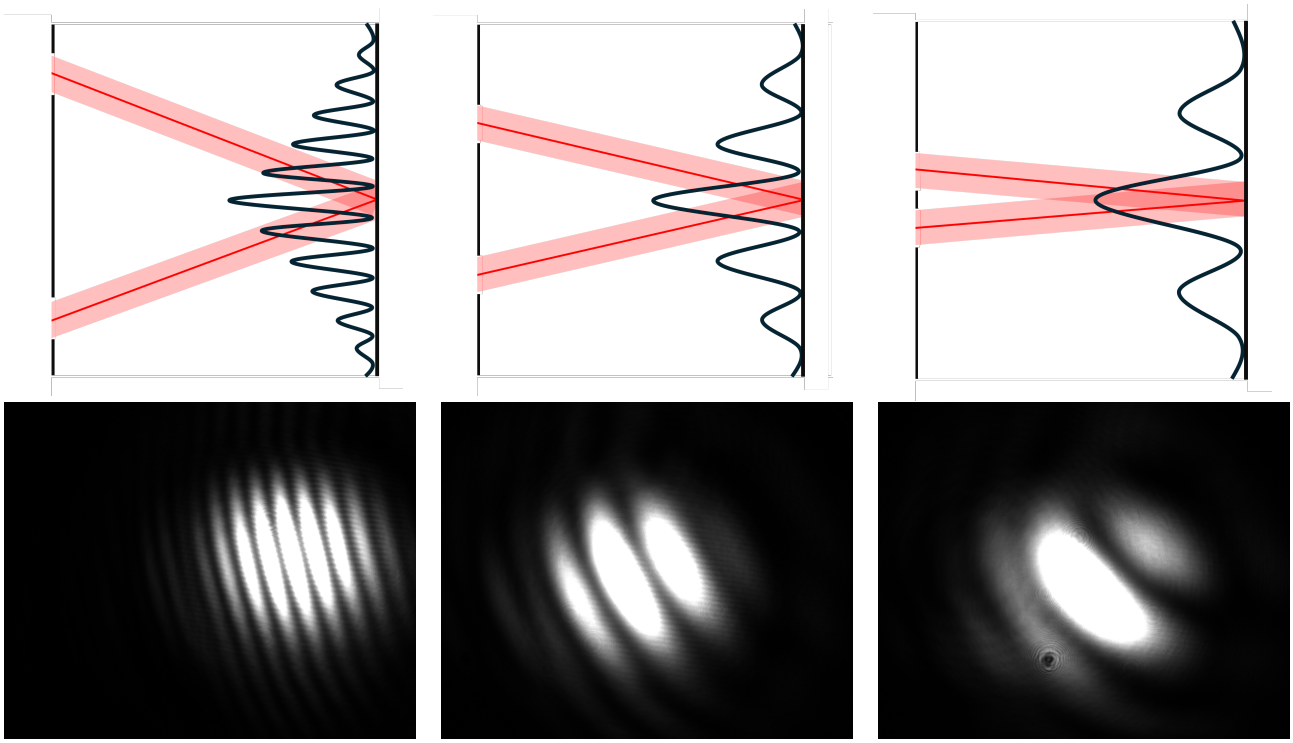

(a) (b) (c)

Figure 2.7: *Interference fringes on camera when there is no frequency difference between the two laser paths.* ***(top)*** *Illustration showing how improving beam overlap leads to larger fringe spacing.* ***(bottom)*** *Beam spot images of fringes for different levels of beam overlap.*

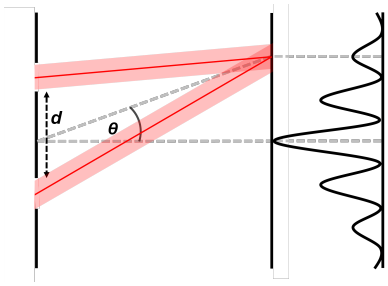

Figure 2.8: *Young's double slit experiment. As the slit distance decreases, the distance between interference spots increases based on Equation 2.5.*

This can be explained using the principle of interference between light from two slits in Young's double slit experiment [32]. By decreasing the slit distance in Figure 2.8, the distance between interference points increases. This is why when the beams in Figure 2.7 become more co-linear, the fringe spacing increases. The distance between the fringes is related to the overlap of the beams (or the distance d between slits in Figure 2.8) by:

$$m\lambda = d\sin\theta \tag{2.5}$$

So by decreasing the distance between the slits (*i.e.* improving the overlap of the beams) $\sin\theta$ (and therefore θ) must increase, meaning the fringe spacing to increase. To obtain a strong beating signal on the detector, the fringe spacing on the camera must be maximized to ensure the beams are as collinear as possible. Once aligned, switching the AOMs back to their original frequencies produces a beating signal on the detector.

2.3.2 Stability

The stability of the SDHM setup is far better than the previous iterations, as seen when comparing previous setups in Figure 2.9 and Table 2.1. The fluctuations in the phase are significantly reduced due to both beams sharing components and a similar path. The only difference in paths occurs in Figure 2.5 where the frequency-shifted beam from the AOM (red) is directed into a second AOM before recombining with the non-frequency-shifted beam (yellow).

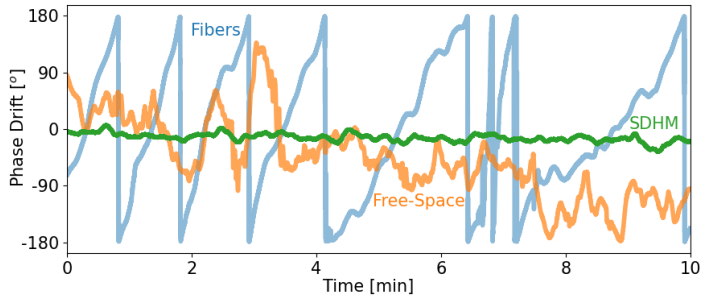

Figure 2.9: *Phase drift with the SDHM setup (green), fiber setup (blue), and previous free space setup (orange). The fiber setup phase is wrapped around* $-180°$ *to* $180°$ *for clarity.*

Setup	Phase Drift	
	[°/min]	[nm/min]
Fibers	284.99	501.10
free space	4.65	8.17
SDHM	1.48	2.61

Table 2.1: *Phase drift for each setup, from the data in Figure 2.9.*

While the SDHM setup is stable enough to measure small phase shifts, the phase modulation of a structure comes from excitons in 2D materials. The optical effects in these materials come primarily from excitons and can be controlled, as described in Section 2.4 below.

2.4 2D Materials and Excitons

2D materials have strong covalent bonds with other atoms in-plane but are only held together by van der Waals forces between each plane. This allows layers to be stripped from the bulk to form very thin (even single-atom-thick) layers of material [33][34]. There is an abundance of examples of materials that can be exfoliated to create monolayers stable at room temperature, including graphene, hBN, and WS_2, with another 1,800 potentially exfoliable materials [35][36][37][38]. Many of these materials have unique properties when they are reduced to monolayer thicknesses compared to their bulk counterparts because of quantum confinement of the electronic wave function within the material and reduced electronic screening from surrounding atoms.

Transition metal dichalcogenides (TMDs) are an example of these 2D materials, which are formed from semiconductors [39]. The optical properties of TMDs are primarily the result of excitons: electron-hole pairs in semiconductors bound by the Coulomb force [40] [41]. An electron-hole pair is formed when a photon excites an electron from the valence band to a vacancy in the conduction band [42]. The energy of the transition is equal to the photon energy:

$$\Delta E = \frac{hc}{\lambda} \tag{2.6}$$

where ΔE is the change in energy due to the transition, $\frac{hc}{\lambda}$ is the photon energy, h is planck's constant, c is the speed of light in vacuum, and λ is the incident photon wavelength [43][44].

Lower electronic screening of the quantum confined excitons in TMDs leads to much larger binding energies than bulk semiconductors and allows for the formation of excitons, rather than electron-hole pairs disassociating into free-charge carriers [45]. The energy of an exciton E_X is related to the band gap energy E_g and the binding energy E_b by Equation 2.7 [46].

$$E_X = E_g - E_b \tag{2.7}$$

After examining Equation 2.7, it's clear that it's energetically favorable to form an exciton rather than free charges; therefore, strong absorption is expected at energies near E_X. The presence of excitons is visible in Figure 2.10, which shows the real and imaginary parts of the refractive index of WS_2 [47]. The increased absorption is seen as a peak in the imaginary part, directly proportional to the absorption coefficient [48]. However, bulk semiconductors with impurities contain excess free charges which screen the Coulomb forces between electron-hole pairs, reducing the binding energy E_b

and leading to lower exciton formation [49].

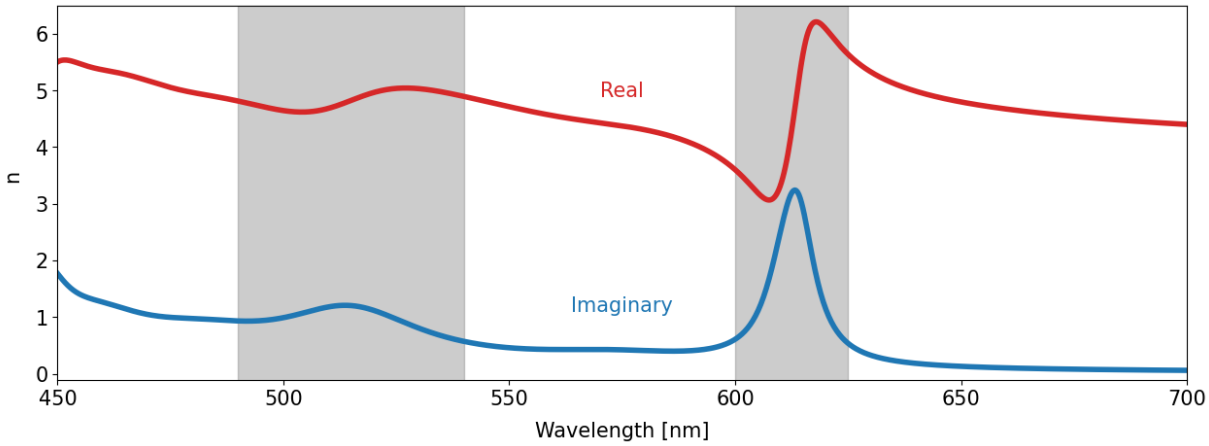

Figure 2.10: *Real (red) and Imaginary (blue) parts of the refractive index of monolayer WS_2 showing the presence of two excitonic resonances [50]. Highlighted in grey are the A exciton* ***(right)*** *and the B exciton* ***(left)****.*

As mentioned, the optical properties of TMDs are dominated by excitons. Materials such as WS_2, WSe_2, MoS_2 and $MoSe_2$ show strong excitons at monolayer thicknesses [51]. This is because the bulk crystal has an indirect band gap, but in monolayer form, this becomes a direct band gap. The reduced electronic screening by surrounding material and quantum confinement of the wave function also make it more likely for an exciton to form and be observed at the exciton wavelength in the emission spectrum.

2.5 Quenching Excitons with Electrical Gating

The presence of an exciton in a material's optical properties depends on the rate of recombination of electron-hole pairs in the material. This rate is reliant on the relative concentrations of both electrons and holes, which can be controlled with a gating voltage. Applying a gate voltage across the monolayer introduces a buildup of excess static charges at the surface, changing the carrier concentrations and the rate of non-radiative recombination of these charges. The introduction of more charges into the sample results in the exciton becoming less dominant in the material's optical properties. This is visible in the refractive index of WS_2 in Figure 2.11.

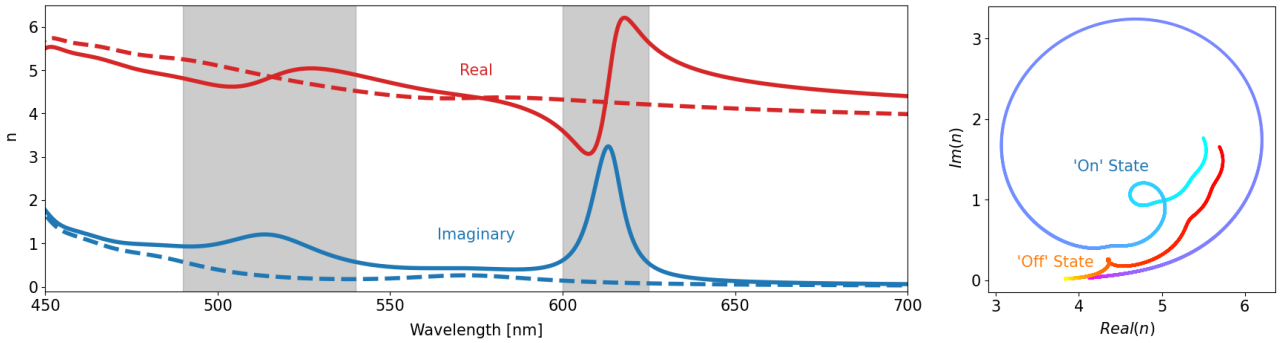

Figure 2.11: ***(left)*** *Real (red)* and Imaginary (blue) parts of the refractive index of WS_2 while applying a voltage to quench the A and B excitons. The solid lines are the refractive index before quenching, and the dashed lines are the refractive index after quenching. **(right)** Plot of the refractive index in the complex plane for 450 nm $< \lambda <$ 700 nm. Each loop in the plot represents an exciton. The exciton disappearing in the refractive index is seen when the two most prominent loops in the "On" state (blue) disappear in the "Off" state (red).

This effect alters the refractive index of the material, thereby affecting the absorption of incident light. As the phase pickup when reflecting off a material changes based on the absorption, then quenching the exciton should change the phase shift of the light that is reflected. This effect can be used to modulate the phase of the reflected light by applying a voltage across a structure with a strong exciton resonance. The stronger the exciton resonance within the structure, the larger the change in refractive index when applying a gate voltage, and therefore the larger the phase difference upon reflection. To measure this, the structure must be designed to exhibit a significant change in the reflection phase when a voltage is applied. The design of this structure is discussed in detail in Section 3.5.

3 Simulating Phase Responses

In this section, the theory behind the transfer matrix method (TMM) will be discussed and applied to calculate the expected changes in phase and amplitude when scanning across samples [52]. The TMM is explained in Section 3.1 to show how the phase of light upon reflection on a surface is simulated, and Section 3.2 shows the predicted response from two incident beams. Finally, Section 3.3 compares the results from the TMM code implementation with literature simulations for verification and Section 3.4 shows the response expected when a sample surface is composed of two different materials.

3.1 Transfer Matrix Method

When an electric field **E** is incident on an interface between materials, there is reflection and transmission of the field at this interface [53]. The amount of light that is reflected or transmitted and the change in the phase of the field are determined by the refractive indices of both materials. These properties can be characterized by the Fresnel coefficients of the interface, r and t, which are the reflection and transmission coefficients, respectively [54]. These coefficients can be written as:

$$r = |r|e^{i\phi_r} \qquad t = |t|e^{i\phi_t} \tag{3.1}$$

where $|r|, |t|$ determine the change in amplitude of the field and ϕ_r, ϕ_t determine the change in phase of the field.

If the field is incident on a single thin film interface, there is only one reflected field and one transmitted field [55]. The change in the reflected or transmitted field is dependent on the incidence angle θ_0 and the polarization of the incident field. The incident light can be either s-polarized, where the electric field **E** is normal to the plane of incidence, or p-polarized, where **E** is parallel to the plane of incidence [56]. The Fresnel coefficients can be calculated using the following definitions:

$$\begin{aligned} &\underline{\textit{S-Polarization}} && \underline{\textit{P-Polarization}} \\ r_s &= \frac{n_0\cos\theta_0 - n_1\cos\theta_1}{n_0\cos\theta_0 + n_1\cos\theta_1} & r_p &= \frac{n_1\cos\theta_0 - n_0\cos\theta_1}{n_1\cos\theta_0 + n_0\cos\theta_1} \\ t_s &= \frac{2n_0\cos\theta_0}{n_0\cos\theta_0 + n_1\cos\theta_1} & t_p &= \frac{2n_0\cos\theta_0}{n_1\cos\theta_0 + n_0\cos\theta_1} \end{aligned} \tag{3.2}$$

Where $n_{0,1}$ is the refractive index of each material and $\theta_{0,1}$ is the angle that the field makes to the normal of the surface within each material.

If the field is incident on a material with a finite thickness instead of a single interface, multiple reflections and transmissions can occur at each interface [57]. By increasing the number of these layers, the number of interfaces also increases, which adds further complexity to this calculation. The transfer matrix method (TMM) deals with this complexity without the need to manually calculate the interaction at each interface [58] [59].

Each layer has a transfer matrix M which describes the output of light as it interacts with the layer and relates the light on one side of the layer to the light on the other side by:

$$\begin{pmatrix} \Psi_R^+ \\ \Psi_R^- \end{pmatrix} = M \begin{pmatrix} \Psi_L^+ \\ \Psi_L^- \end{pmatrix} \tag{3.3}$$

where Ψ_L, Ψ_R represent the waves on the left and right of the sample, respectively, and Ψ^+, Ψ^- represent the waves traveling to the right and the left, respectively.

By combining the matrices for each layerM_n, the transfer matrix for the entire structure $\tilde{M}$ can be realized. For given layer thickness (δ_n) and the Fresnel coefficients at the interface between one layer and the next ($r_{n,n+1}, t_{n,n+1}$), the transfer matrix for any layer is given by Equation 3.4.

$$M_n = \begin{pmatrix} e^{-i\delta_n} & 0 \\ 0 & e^{i\delta_n} \end{pmatrix} \begin{pmatrix} 1 & r_{n,n+1} \\ r_{n,n+1} & 1 \end{pmatrix} \frac{1}{t_{n,n+1}} \tag{3.4}$$

Calculating this matrix for every layer in a structure of N layers allows $\tilde{M}$ to be determined:

$$\begin{aligned} \tilde{M} &= \frac{1}{t_{0,1}} \begin{pmatrix} 1 & r_{0,1} \\ r_{0,1} & 1 \end{pmatrix} M_1 M_2 \cdots M_{N-2} \\ &= \begin{pmatrix} \tilde{M}_{00} & \tilde{M}_{01} \\ \tilde{M}_{10} & \tilde{M}_{11} \end{pmatrix} \end{aligned} \tag{3.5}$$

Here, the first two terms are due to the first interface, and the M_n terms are for every other interface within the structure. From Equation 3.5, the definition of the Fresnel coefficients is:

$$r = \frac{\tilde{M}_{10}}{\tilde{M}_{00}}; \quad t = \frac{1}{\tilde{M}_{00}} \tag{3.6}$$

For the simulations used in this thesis, a TMM Python package is used to calculate the reflectivity coefficient for various structures [60] [61].

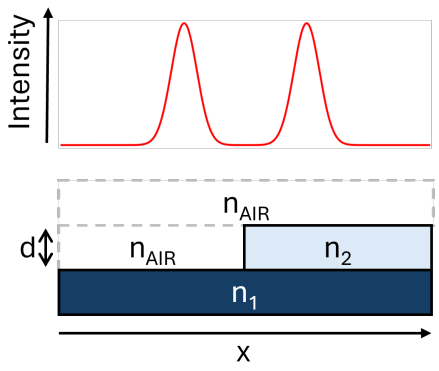

Figure 3.1: ***(bottom)*** *Structure given to the TMM function to calculate the reflectivity coefficient r in Equation 3.6.* ***(top)*** *Gaussian profile for two beam spots.*

As the experiments involve scanning the incident lasers from one structure to another, the simulations need to replicate this process. The goal of these simulations is to create a plot of phase as a function of position, where the surface height and material changes at some point along the position range. To do this, the following procedure is implemented:

1. Each laser spot is given a Gaussian profile determined using Equation 3.7. The amplitude of each beam is E_0 and the beam width ω_0 is determined by the numerical aperture (NA) of the objective being used. The distance between the center of each beam is δ [62].

$$E(x, \delta) = E_0 e^{-\frac{(x \pm 0.5\delta)^2}{\omega_0^2}}, \qquad \omega_0 = \frac{0.61\lambda}{\mathrm{NA}} \tag{3.7}$$

2. The structure, seen in Figure 3.1, is created using two arrays, one with thicknesses and another with refractive indices. Every element in the arrays represents an x-position with particular refractive indices and thicknesses for the materials present there. These arrays are used to calculate the reflection coefficient r at every position.

3. The beam spot amplitudes at each x-position are multiplied by r at that position, generating a new 'reflected' array for each beam, which is integrated over all positions ($L(x, \delta)$) to calculate

the response $D(x, \delta)$ for each position x, as in Equation 3.8 [63]:

$$L_{1,2}(x, \delta) = \int E_{1,2}(x, \delta) \cdot r(x)$$
$$D(x, \delta) = L_1(x, \delta) \cdot L_2^*(x, \delta). \tag{3.8}$$

4. The response $D(x, \delta)$ is a complex value for each position in the form $D(x, \delta) = |D|e^{i\phi_D}$ [64]. Taking the amplitude $|D|$ and argument ϕ_D gives the amplitude and phase responses due to reflection at that position. This is repeated by scanning the beams across the structure (*i.e.* repeat for every x-position) to determine the changes in amplitude and phase across a structure, as seen in Section 3.2.

The approach to this implementation is based on literature applying the same technique [23][63]. The following section details the simulated responses for two beams incident on the surface of a stepped sample.

3.2 Amplitude and Phase Responses

To calculate the responses from a sample for the common path scheme in Figure 2.5, the simulation procedure in Figure 3.1 is implemented for a step on a sample surface. Since each beam is incident on the sample, both are affected by the sample's reflectivity r given in Equation 3.9, where $r_{1,2}$ are the Fresnel reflectivity coefficients for each material. $|r_n|$ describes the change in amplitude and ϕ_n describes the change in phase reflecting off material n. The initial phase of the beam before reflection is defined as zero for simplicity in the math. In reality, the experiments measure a *change* in the phase, so the phase before reflection is ambiguous.

$$r_1 = |r_1|e^{i\phi_1} \qquad r_2 = |r_2|e^{i\phi_2} \tag{3.9}$$

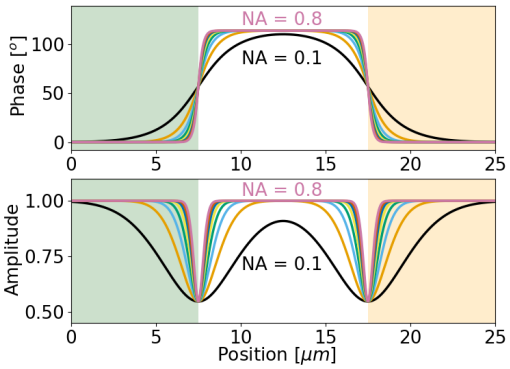

Figure 3.2: *Phase* ***(top)*** *and Amplitude* ***(bottom)*** *responses with two incident beams scanning over an edge of a stepped material. In this case, the substrate and step are made from the same material.*

This means that as the beams are moved across an interface, it will result in changes to both reflected beams. However, since the phase of the beat signal depends on the $difference$ in phase between each beam, this technique should only measure a change in phase when the beams are incident on different materials (*i.e.* scanning over a step). This is the SDHM technique being implemented in Figure 2.5, where the gradient of the phase across the surface is being measured [23]. There are three different cases (as seen in Figure 3.2) that can occur as the two beams scan across a stepped interface:

- Both beams are incident on material 1 ($I_{\text{Beat},1}$) in green
- Each beam is incident on a different material ($I_{\text{Beat},1,2}$) in white
- Both beams are incident on material 2 ($I_{\text{Beat},2}$) in orange

Using Equation 2.4, where now each beam is reflected from the sample surface, the following equations for the beating signal are derived:

$$I_{\text{Beat},1} \propto |r_1|^2 AB.Cos(\Delta\omega.t)$$
$$I_{\text{Beat},1,2} \propto |r_1||r_2|AB.Cos(\Delta\omega.t + \Delta\phi_{1,2})$$
$$I_{\text{Beat},2} \propto |r_2|^2 AB.Cos(\Delta\omega.t). \tag{3.10}$$

As mentioned previously, the phase when both beams are incident on the same material is defined as zero since both are experiencing the same phase shift upon reflection. Based on Equations 3.10, when both beams are on the same material, the phase should be zero, and when each beam is on a different material (*i.e.* crossing the interface), the phase should reach a maximum or minimum. The amplitude should drop each time a beam crosses the interface, as the constructive and destructive interference between the beams will vary during this transition. The phase and amplitude responses during these transitions can be seen in Figure 3.2. The steepness of the transition is determined by the beam spot size, where higher NA (and therefore smaller spot size) leads to a sharper phase and amplitude change. In reality, the transition may not become as sharp as Figure 3.2 for higher NA due to the influence of an increasing number of incidence angles. In these simulations, only normally incident light is considered.

The relationship between the amplitude A of an electromagnetic (EM) wave and its intensity I is given by $I \propto A^2$. Therefore, the amplitude of the beating signal, as seen in Equation 3.10, can be written as:

$$|I_{\text{Beat}}| \propto AB \propto \sqrt{I_1 I_2} \tag{3.11}$$

where I_1,I_2 are the intensities of the individual beams that interfere to form the beating signal.

Suppose each beam is now incident on a sample and reflected, using the Fresnel coefficients for reflection $r_{m,n}$. In that case, the intensity of the beating signal becomes $I_{\text{Beat}} = |r_m|A\ |r_n|B$, where $r_{m,n}$ is the reflection coefficient for material m, n. If both beams are incident on the same material, then $m = n$. So the change in intensity upon reflection for each case described above is:

$$\begin{aligned} |I_{\text{Beat},1}| &\propto |r_1|^2 AB \\ |I_{\text{Beat},1,2}| &\propto |r_1||r_2| AB \\ |I_{\text{Beat},2}| &\propto |r_2|^2 AB \end{aligned} \tag{3.12}$$

A and B are the same for all cases (as they are the amplitudes before reflection, and assumed to be constant), so when finding the expected change in amplitude, they cancel out to give:

$$\Delta|I_{\text{Beat}}| = \frac{|I_{\text{Beat},1}|}{|I_{\text{Beat},2}|} = \frac{AB|r_1|^2}{AB|r_2|^2} = \frac{|r_1|^2}{|r_2|^2} \tag{3.13}$$

When comparing the change in amplitude before and after crossing the boundary between materials. The change in amplitude while the beams are traversing the boundary is given by:

$$\Delta|I_{\text{Beat}}| = \frac{|I_{\text{Beat},1,2}|}{|I_{\text{Beat},n}|} = \frac{|r_1||r_2|}{|r_n|^2} \tag{3.14}$$

where $|r_n|$ is the reflection coefficient for either material.

So, the change in amplitude of the beating signal when going from one material to another is proportional to the square of the ratio of the reflection coefficients for each material, as in Equation 3.13 or Equation 3.14. The results in Figure 3.2 are for a stepped surface where the substrate and step are the same material. Therefore, after each transition, the amplitude returns to 1 as expected. For scenarios where the stepped material is different from the substrate, as in Section 3.4 later, the amplitude after each transition will not return to 1 if the reflectances are different. Therefore, by knowing the reflectance of the reference substrate, we can calculate the reflectance of the sample. For the experimental results shown in Chapter 4, only Equation 3.13 is used to analyze the amplitude changes.

The phase change of the incident light can be calculated using TMM [58]. Both beams are incident on the sample, so both acquire a phase pickup upon reflection. Defining the change in phase for each

wave as ϕ_1 and ϕ_2, the change in the beating signal phase $\Delta\phi_{i,j}$ is:

$$\Delta\phi_{i,j} = \phi_i - \phi_j. \tag{3.15}$$

If both waves are reflecting off the same material, $\phi_i = \phi_j$ so $\Delta\phi_{i,j} = 0$. If each wave reflects off a different material, then the phase pickup for each will depend on the reflectivity of that material, as in Figure 3.2. From this, it's clear that the phase should only change when the beams are crossing the border between materials and not when they are moving across the same material.

The simulation in Figure 3.2 shows the amplitude and phase response for a simple stepped structure. However, this model is also tested for more complicated structures and different beam separations to ensure it provides the correct solution to a variety of topologies. The following section tests the model's versatility with reference to the literature.

3.3 Comparing Simulations to Literature

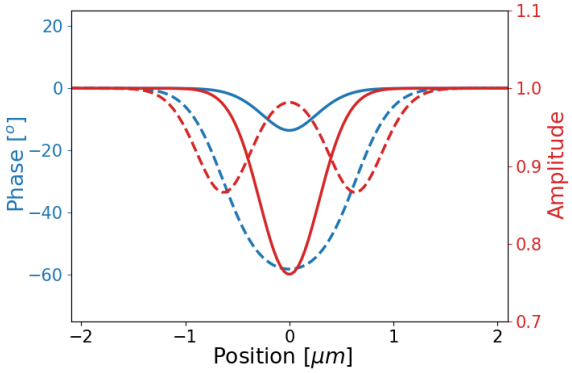

(a)

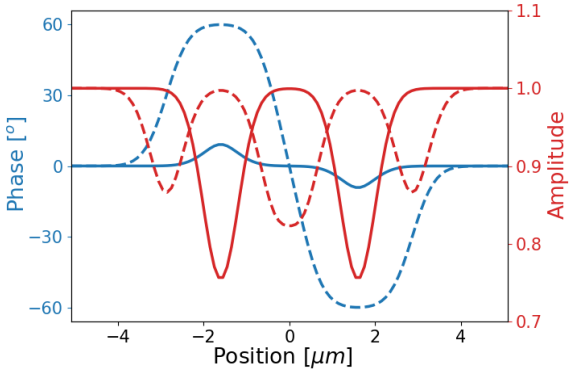

(b)

Figure 3.3: *Amplitude (red) and phase (blue) responses for (a) 60^o phase step and (b) 60^o phase block (width = 5λ). The beam separations for the solid and dotted lines are δ = 0.25λ, 4λ, respectively.*

Recreating the results from previous papers that also implement SDHM is a reliable approach to ensure the model's validity [23] [63]. For testing, four different structures are generated using the approach described in Figure 3.1. The first two are a stepped surface (similar to Figure 3.2) and a block (or simply, a step up and then back down). Both of these structures are designed to have ϕ=60° and reflectance $|r|^2$=1. The remaining two structures are phase gradient metasurfaces, where each unit cell of period Λ contains 6 steps in the range $-180° < \phi < 180°$. The responses can be seen in Figures 3.3, 3.4. Each of these responses comes from scanning two Gaussian beams, with profiles given from Equation 3.7 in Figure 3.1, NA= 0.6 and varying the separation δ between the beams [63]. λ = 633 nm for all results.

Figure 3.3 shows the difference in responses (amplitude and phase) when scanning over the step and block for $\delta = 0.5\lambda$ and $\delta = 4\lambda$. By separating the beams, the transition over an interface changes. For large δ, the phase reaches the true phase difference, and the amplitude contains two distinct dips for every interface (the block only has three dips instead of four, as the block is thin enough that the laser beams interact with both edges simultaneously). For small δ, the beams overlap, which means each beam interacts with the interface at the same time, resulting in a lower phase than the true phase difference and fewer dips in the amplitude.

The responses for the phase gradient metasurfaces (phase responses only) with unit cell periods $\Lambda = 4\lambda$ and $\Lambda = 30\lambda$ (Figure 3.4) are shown for various δ values. These responses follow the same trend as Figure 3.3, where larger δ produces a phase closer to the true phase difference. There is

an interesting effect in the metasurface responses where the constantly increasing phase steps lead to a constant phase difference (Figure 3.4a) when the beam widths are much larger than the step width. However, by increasing the step width (by increasing Λ) then the phase is no longer constant going over the unit cell. Instead, there are oscillations with a magnitude that increases as the beam separation increases. This occurs as the phase response for a single beam is averaged over the entire beam area. If the beam is much larger than the step width, the average stays the same as it scans over the whole structure.

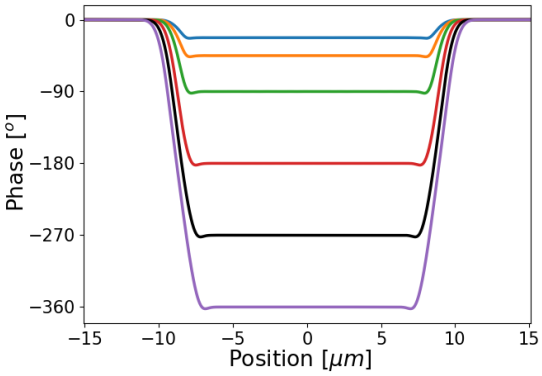

(a)

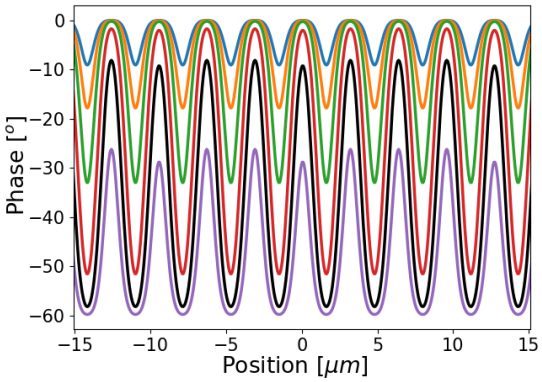

(b)

Figure 3.4: *Phase responses for phase gradient metasurfaces with period (a)* $\Lambda = 4\lambda$ *and (b)* $\Lambda = 30\lambda$. $\delta = 0.25\lambda, 0.5\lambda, \lambda, 2\lambda, 3\lambda, 4\lambda$ *(blue* $\rightarrow$ *violet).*

Overall, the results in the literature strongly agree with the simulations in Figures 3.3, 3.4. The model is established to work for a variety of structure topologies, including simple steps and blocks, to more complicated phase gradient metasurfaces.

From the results in Figures 3.3, 3.4, it is clear that moving the beams closer together leads to the phase peak being lower than the true structural phase jump if the distance between the beams is smaller than the beam width. Figure 3.5 shows how the value of this peak changes as the beam separation δ is reduced, where the minimum beam separation while still measuring the true phase value is approximately 10 μm. For all measurements performed with $\lambda = 633$ nm, the beams were maintained at separations larger than this.

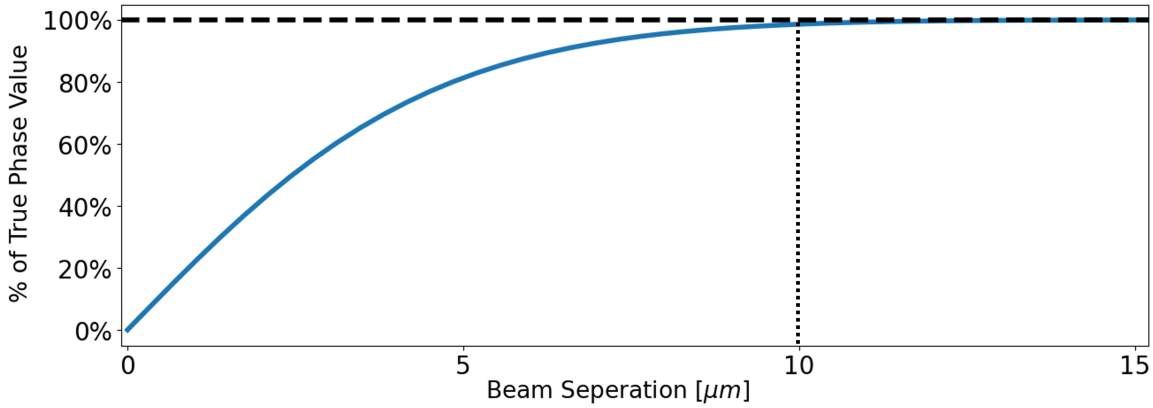

Figure 3.5: *Change in phase peak value as beam spots are brought closer together. This is done for* $\lambda = 633$ *nm and NA*$= 0.6$.

3.4 Simulating Different Material-Substrate Samples

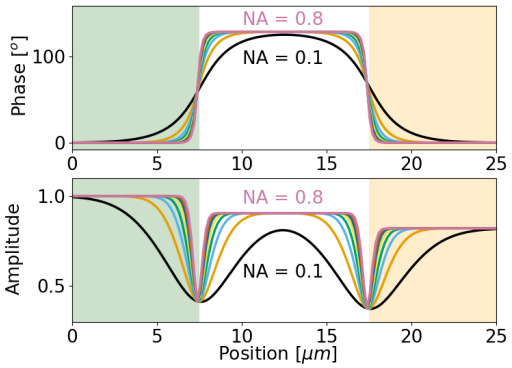

Figure 3.6: *Phase **(top)** and Amplitude **(bottom)** responses with two incident beams scanning over an edge of 100 nm TiO_2 on Si.*

For the amplitude and phase responses in Figure 3.2, the structure being simulated is a Si substrate with a 100 nm step, also of Si. However, in this thesis, the samples being used are substrates with a different material for each step. In those cases, the response is different from the amplitude and phase plot in Figure 3.2. The response for a 100 nm TiO_2 sample on a Si substrate, for example, is shown in Figure 3.6, where now the amplitude does not return to 1 as the reflectivity of TiO_2 is lower than Si ($R_{TiO_2} \approx 0.2$, $R_{Si} \approx 0.4$ for $\lambda = 633$ nm).

While the response for different combinations of materials will be different for each case, the overall trend is still apparent. The phase always forms a peak when one of the beams is crossing over an interface, but returns to the original phase value as the other beam crosses over. The magnitude of this peak is found using Equation 3.15. The amplitude will form a step-like shape as each beam crosses the edge, where the step height, given by Equations 3.13, 3.14, depends on the ratio of reflectivities of both materials. If the technique being used only utilizes one incident beam instead of two, the equations from Section A.3 are used instead to find the phase peak and amplitude step heights.

3.5 Optimizing Structure Design for Maximum Phase Modulation

As mentioned, to measure the phase difference upon reflection due to changes in a material's excitonic resonance, a structure is designed to maximize the phase shift. Following the work of Epstein, the choice of active structure is a monolayer WS_2 sandwiched between two hBN flakes on top of an Au contact [65]. The contact is necessary for applying the gate voltage, and the bottom hBN layer is essential for insulating the WS_2 from one of the contacts.

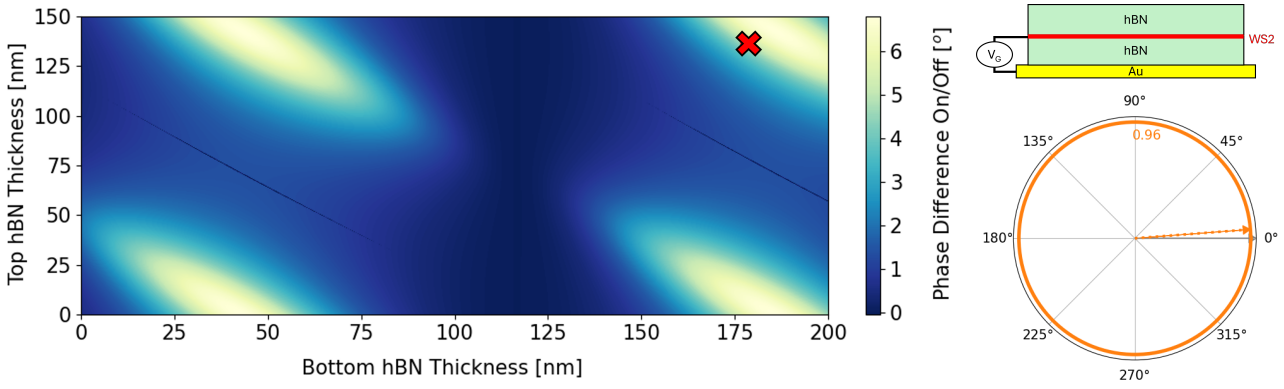

Figure 3.7: ***(left)** Phase difference for WS_2 exciton in On-Off states upon reflection of a hBN - WS_2 - hBN - Au structure **(right, top)**. The choice of thicknesses for the hBN is marked with a "X". The polar plot **(right, bottom)** shows the change in amplitude and phase (orange) compared to the phase before modulation (solid-grey vector).*

Changing the thicknesses of the hBN flakes changes the phase shift detected when the light is reflected from the structure, due to the Fabry-Perot interference increasing the field intensity within the WS_2 monolayer [66].

This increase in field intensity leads to higher absorption, which results in a change in the reflection phase [67]. Therefore, the thicknesses need to be optimized to produce the largest phase difference between the "On-Off" states for the structure, and TMM package in Section 3.1 is used to determine the optimal thicknesses to achieve this. Using the structure: hBN → WS_2 → hBN → Au, the TMM package calculates the reflectivity coefficient for various combinations of hBN thicknesses, and the optimal phase difference is determined from Figure 3.7. Based on the thicknesses available from exfoliation, the structure is built with the following thicknesses for hBN: $d_{\text{Top}} = 137$ nm, $d_{\text{Bottom}} = 177$ nm. With incident light at $\lambda = 633$ nm, the estimated change in the reflected light is $\phi = 4.97°$ and $\Delta|I_{\text{Beat}}| = 0.95$.

The change of reflection phase can also be illustrated with the plot of the reflection coefficient of the active structure in the complex plane in Figure 3.8a. The expected change in reflection response for this structure between the "On-Off" states is a phase change of $\Delta\phi = 4.62°$ and an amplitude change of $\Delta|I_{\text{Beat}}| = 0.95$.

Unfortunately, after the structure is finalized, the laser at $\lambda = 633$ nm stopped working. As a result, a different wavelength laser is used to measure the phase modulation. The change in reflection response at the new laser wavelength, $\lambda = 532$ nm, is shown in Figures 3.8b, 3.9. The phase and amplitude change for modulation at this new wavelength is expected to be $\phi = 0.48°$ and $\Delta|I_{\text{Beat}}| = 0.98$ for $\lambda = 532$ nm. While the expected phase shift during modulation is not large, the structure is tested in Chapter 4 with various gating voltages. The results can be seen in Section 4.3.2.

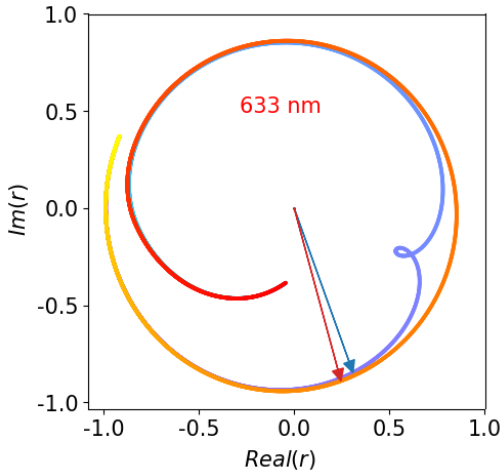

(a)

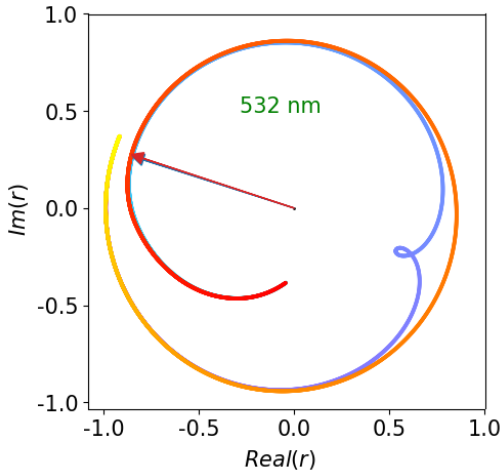

(b)

Figure 3.8: *Reflection coefficient r in the complex plane before (blue) and after (red) exciton quenching for the active structure. The arrows represent the reflection phase vector for each state, with incident light (a) $\lambda = 633$ nm and (b) $\lambda = 532$ nm.*

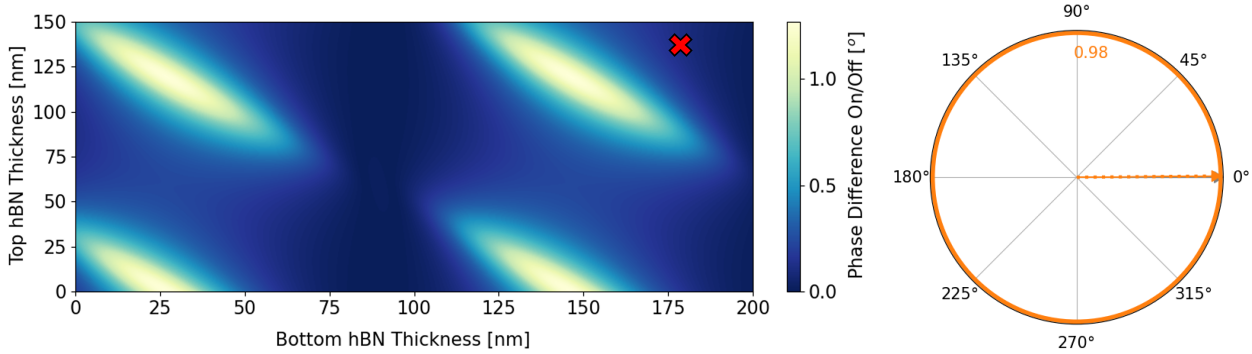

Figure 3.9: ***(left)*** *Comparison of maximum phase difference between "On-Off" states. The "X" denotes what hBN thicknesses are used to demonstrate how large the expected structure phase shift during modulation is compared to the maximum (bright green spots).* ***(right)*** *Polar plot of phase vector upon reflection (dashed, orange) compared to before incidence (solid, grey).*

4 Phase Measurements

This section details the experiments performed to determine the accuracy of the SDHM setup described in Section 2.2.3 when compared to the simulations in Section 3.3. Several different samples are tested, each providing a smaller phase shift or using a transparent substrate to fully characterize the measurement capabilities. The samples are also measured with two incident wavelengths, a HeNe 633 nm laser and a 532 nm fiber-coupled diode laser. After benchmarking the setup with these different samples and lasers, the active structure designed in Section 3.5 is fabricated and tested, with the results displayed in Section 4.3.2.

4.1 Benchmarking System with $\lambda = 633$ nm

Section 3 shows simulated results that are supported by literature using a similar technique [63]. The next step is to use the setup in Figure 2.5 to measure the changes in amplitude and phase of the reflected light experimentally and compare the results with simulations. The three initial samples are TiO_2, SiO_2 and Au-Cr. Each film is on a Si substrate, and the measurements are performed by scanning the laser spots from Si to the material film. The choices of material were decided on the basis of the calculated phase shifts that each material should produce when scanning the edge. A 60 nm TiO_2 film on a Si substrate is expected to produce a 66° phase shift, while 92 nm SiO_2 and 32 nm - 3 nm Au-Cr films on Si are expected to produce 29° and 11°, respectively. The expected phase shift is smaller for each subsequent sample, and as such, these samples are used to determine whether a phase shift of the order of 10° is detectable. The results for each sample are shown in 4.1.

The left column in Figure 4.1 is the phase (top) and amplitude (bottom) as a function of position on the sample. The experimental results are shown (solid-black line) with the error (light-blue) around the data. The error is calculated by finding the mean and standard deviation across 8 scans for the same start and end positions. The simulations for each plot are shown in dotted lines. These experimental results in Figure 4.1 and Table 4.1 agree well with the simulations. Measurements of phase shift $\phi \approx 10^o$ are possible with considerable accuracy. The results also show that with a high-reflectance substrate ($R_{Si} \approx 0.35$) the measurements can be reproduced consistently, as larger intensity makes measurements less susceptible to noise [68]. Any differences between the simulations and experiments are likely due to a non-ideal Gaussian spot, slight irregularities in the sample surface or interface, and potential noise around the system.

The right column shows the same results in polar form. The solid-grey vector at $\phi = 0^o$ represents the phase of the light on the substrate as a reference, and the solid-green and dotted-orange vectors are the experimental and simulated results, respectively. The angle of each vector with respect to the grey vector represents the phase change of the light upon reflection and the length of the vector represents the change in amplitude. In these cases, the phase is the difference in phase as one beam travels over the edge of the sample while the other remains on the substrate, and the amplitude represents the total change in amplitude when both beams are on the sample versus when both beams are on the substrate. The substrate vector (solid-grey) has $\phi = 0^o$ and $|E| = 1$. The results from Figure 4.1 are also tabulated in Table 4.1.

The measurements with a high-reflectance substrate show good agreement with simulations. The inaccuracies between simulations and experimental results could be due to differences in the sample step or noise in the system. The sample is simulated as a perfect step between materials, as seen in the insets. However, it's possible that the cross-section of this interface is not optimal, or that the height is 1-2 nm different from the simulated cases. This height difference would alter the measured phase due to a difference in the propagation phase accumulated when reflecting from the substrate.

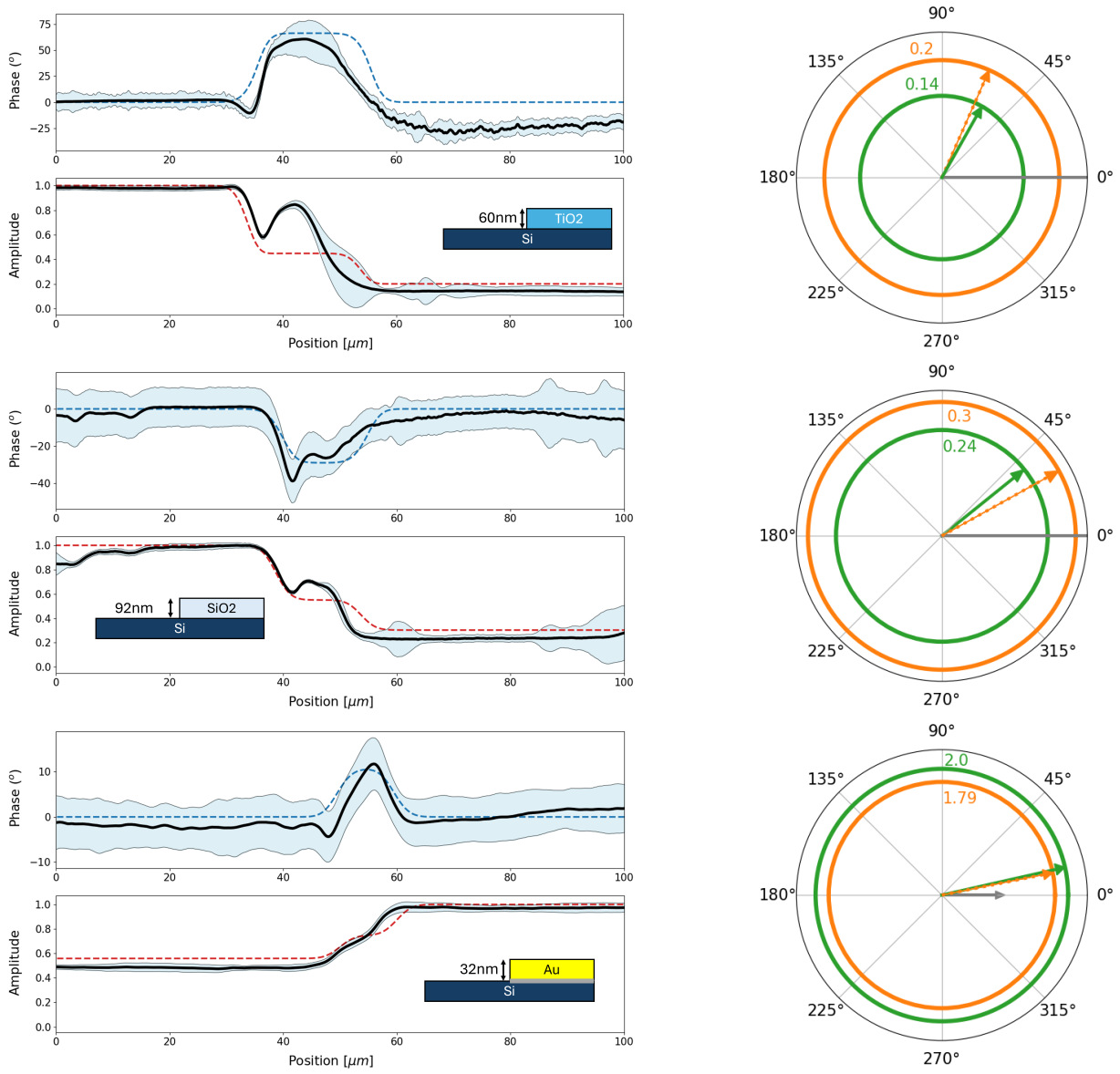

(a) (b)

Figure 4.1: *Experimental results ($\lambda = 633$ nm) compared to simulations for TiO_2* ***(top)****, SiO_2* ***(middle)****, and Au-Cr* ***(bottom)*** *on Si substrate. (a) Phase and amplitude changes while scanning over the edge of the sample. (b) Polar plots of the reflection vector for experimental data (solid-green) and simulation (dotted-orange). A schematic of the sample is included in the inset of each plot.*

TiO_2	Sim	Exp	SiO_2	Sim	Exp	Au - Cr	Sim	Exp
$\Delta\lvert I_{\text{Beat}}\rvert$	0.20	0.14 ± 0.05	$\Delta\lvert I_{\text{Beat}}\rvert$	0.30	0.24 ± 0.05	$\Delta\lvert I_{\text{Beat}}\rvert$	1.79	2.00 ± 0.03
$\Delta\phi$	66.20°	$60.57° \pm 8.21°$	$\Delta\phi$	29.07°	$38.88° \pm 11.26°$	$\Delta\phi$	11.36°	$12.70° \pm 5.31°$

Table 4.1: *Simulated and experimental results for TiO_2, SiO_2 and Au-Cr on Si substrate. $\lambda = 633$ nm.*

However, the signal strength for samples on transparent substrates (e.g., SiO_2, where $R_{SiO_2} \approx 0.03$) is much weaker and is therefore much more influenced by noise from thermal fluctuations. Samples with a transparent material substrate (SiO_2) are used to determine the accuracy with a weaker reflected signal, including a sample with graphene on a Si-SiO_2 substrate as the expected phase shift is $\phi < 2°$. This serves as a test to determine if phase shifts of $\phi \approx 1°$ are observable for this system. The layout of the results in Figure 4.2 and Table 4.2 is the same as before. These results show less agreement

with simulations than the previous samples. A possible explanation for this is the decreased intensity of the reflected laser spots, resulting in the signal I_{Beat} being noisier. Also, as seen in Figure 4.2, there are oscillations in the phase and amplitude for the graphene measurements. This may be due to very small changes in the sample height during the scanning that introduce periodic noise into the signal. While efforts are made to remove this noise as much as possible, there are still artifacts present in the final plots.

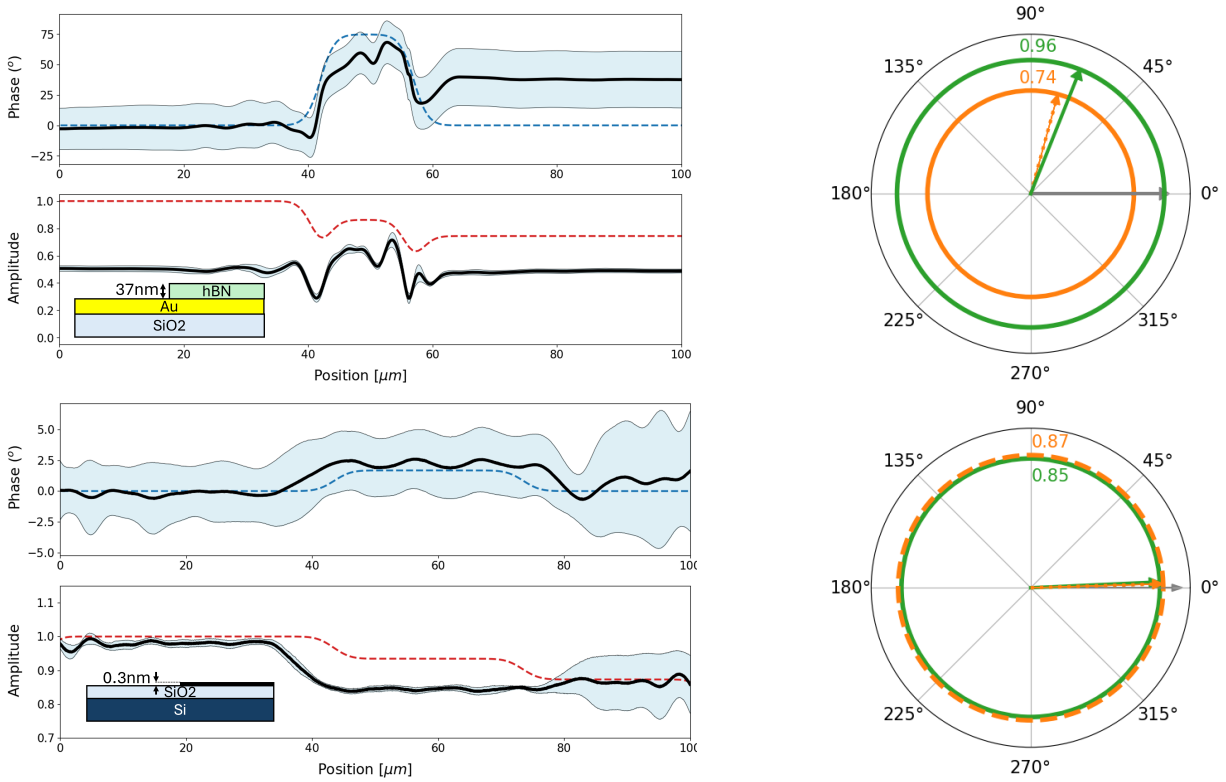

(a) (b)

Figure 4.2: *Experimental results ($\lambda = 633$ nm) compared to simulations for hBN on Au-SiO_2 substrate* ***(top)****, and C* ***(graphene, bottom)*** *on SiO_2-Si substrate. (a) Phase and amplitude changes while scanning over the edge of the sample. (b) Polar plots of the reflection vector for experimental data (solid-green) and simulation (dotted-orange). A schematic of the sample is included in the inset of each plot.*

37nm *hBN*	Sim	Exp
$\Delta\lvert I_{\text{Beat}}\rvert$	0.74	0.96 ± 0.02
$\Delta\phi$	74.72°	$68.29° \pm 20.00°$

0.31nm *C*	Sim	Exp
$\Delta\lvert I_{\text{Beat}}\rvert$	0.87	0.85 ± 0.02
$\Delta\phi$	1.67°	$2.58° \pm 2.75°$

Table 4.2: *Simulated and experimental results for hBN on Au-SiO_2 substrate, and C on SiO_2-Si substrate.*

While these results agree less with the simulations, the results from the graphene sample suggest phase shifts $\phi \approx 1°$ are within the detectable range. Although the noise is of the order of $> 5°$ for most samples, the graphene sample can be measured with a phase shift less than this. This is possible by decreasing the time constant for the lock-in amplifier to become more sensitive to small phase changes. The downside of this is that the phase is also more susceptible to other sources of noise, such as oscillations in the sample position as seen in the graphene measurement in Figure 4.2. The oscillations can be filtered out by performing a Fourier Transform to block the noise frequency, isolating the small phase shift detected from graphene [69]. This oscillating noise is not seen in the other samples due to the higher time-constant and faster sample movement velocity.

4.2 Benchmarking Samples with $\lambda = 532$ nm

Due to an issue with the 633 nm HeNe laser (discussed in a later section), the remaining measurements were taken with a $\lambda = 532$ nm laser source. This source provides the opportunity to measure samples with a different incident wavelength. Figure 4.3 and Table are the same benchmark samples measured with the $\lambda = 532$ nm (*i.e.* TiO_2, SiO_2 and Au-Cr on Si substrates). As before with $\lambda = 633$ nm, the experimental results for these samples agree well with the simulated results. The high reflectivity of the materials is favorable for measurements where $\phi \approx 10°$.

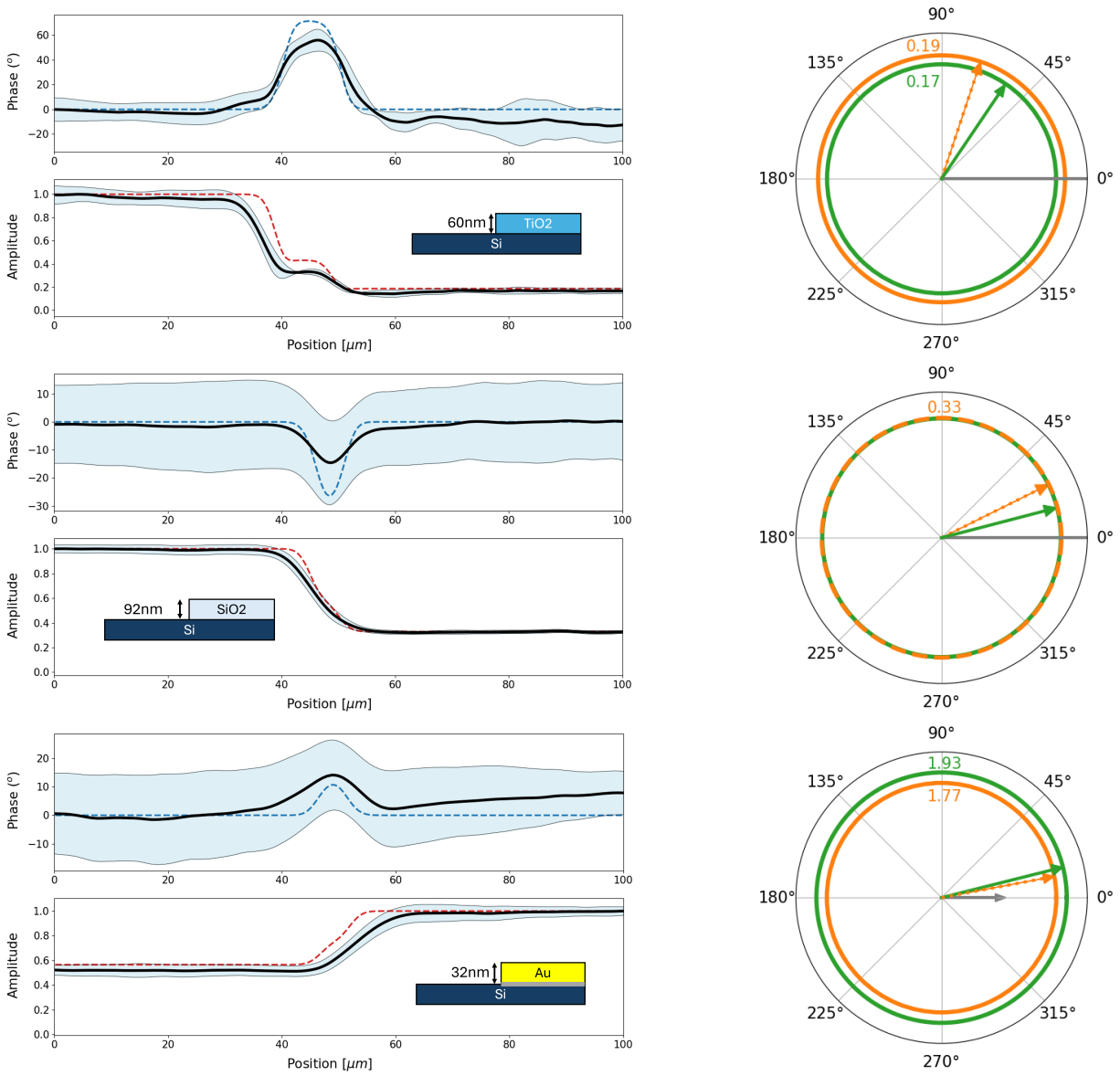

(a) (b)

Figure 4.3: *Experimental results ($\lambda = 532$ nm) compared to simulations for TiO_2* ***(top)****, SiO_2* ***(middle)****, and Au-Cr* ***(bottom)*** *on Si substrate. (a) Phase and amplitude changes as scanning over the edge of the sample. (b) Polar plots of the reflection vector of experimental data (solid-green) compared to simulation (dotted-orange). A schematic of the structure being studied is included in the inset of each plot.*

TiO_2	Sim	Exp	SiO_2	Sim	Exp	Au-Cr	Sim	Exp
$\Delta\lvert I_{\text{Beat}}\rvert$	0.19	0.17 ± 0.04	$\Delta\lvert I_{\text{Beat}}\rvert$	0.33	0.33 ± 0.03	$\Delta\lvert I_{\text{Beat}}\rvert$	1.77	1.93 ± 0.05
$\Delta\phi$	71.30°	$55.95° \pm 9.48°$	$\Delta\phi$	26.41°	$14.60° \pm 14.40$	$\Delta\phi$	10.67°	$14.08° \pm 12.87°$

Table 4.3: *Simulated and experimental results for TiO_2, SiO_2 and Au-Cr on Si substrate. $\lambda = 532$ nm.*

This confirms the reliability of the measurements to detect accurate phase shifts while scanning over the edge of a material. There are sources of error in the process of scanning, such as defects on the sample and vertical changes on the sample holder while moving (seen for graphene measurements in Figure 4.2). These errors can be ignored when measuring phase modulation in a gated structure by maintaining the sample at a fixed position and adjusting the gating voltage. This process is described in Section 4.3.

4.3 Active Structure Experiments

In this section, the fabrication of the finalized structure design from Section 3.5 is described. Once complete, the sample is tested with various gating voltages while monitoring the phase.

4.3.1 Device Fabrication

To fabricate the structure, a batch of hBN flakes is exfoliated and searched to find any that have thicknesses matching the values selected in Figure 3.7. A WS_2 sample is also selected, ensuring it's large enough to be used in the structure by checking the photoluminescence for any cracks [70]. This allows for the selection of the largest monolayer flake to increase the surface contact area on the Au contact probes. The components are stacked together and constructed, with the separate components and the final structure shown in Figure 4.4 [71].

Before measuring phase shifts, the structure is tested to ensure the exciton is still prominent and can be quenched with a gate voltage. Measuring the photoluminescence (PL) of the structure shows the exciton at the wavelength expected from Figure 2.11. Repeating this measurement for various gating voltages in Figure 4.5 shows the PL at the exciton wavelength reducing as the voltage is increased from -25V to 25V. The reflectivity of the structure at each voltage also demonstrates the effects of exciton quenching. The reflectivity for the A and B excitons is plotted next to the simulated reflectivities (black) in Figure 4.5.

The plots in Figure 4.5 confirm the presence of the A and B excitons in the device and establish that by applying a gating voltage, the excitons are quenched. The differences in reflectivity to simulations could be due to the defects present on the surface of the Au contact that form an air pocket in the structure. This is seen in Figure 4.4e next to the laser spots. Another possibility is the shifting of material on the surface of the structure when different voltages are applied. Slight fluctuations in the reflectivity are observed when being measured, which could indicate movement of defects on the surface due to the excess charge buildup or even thermal changes.

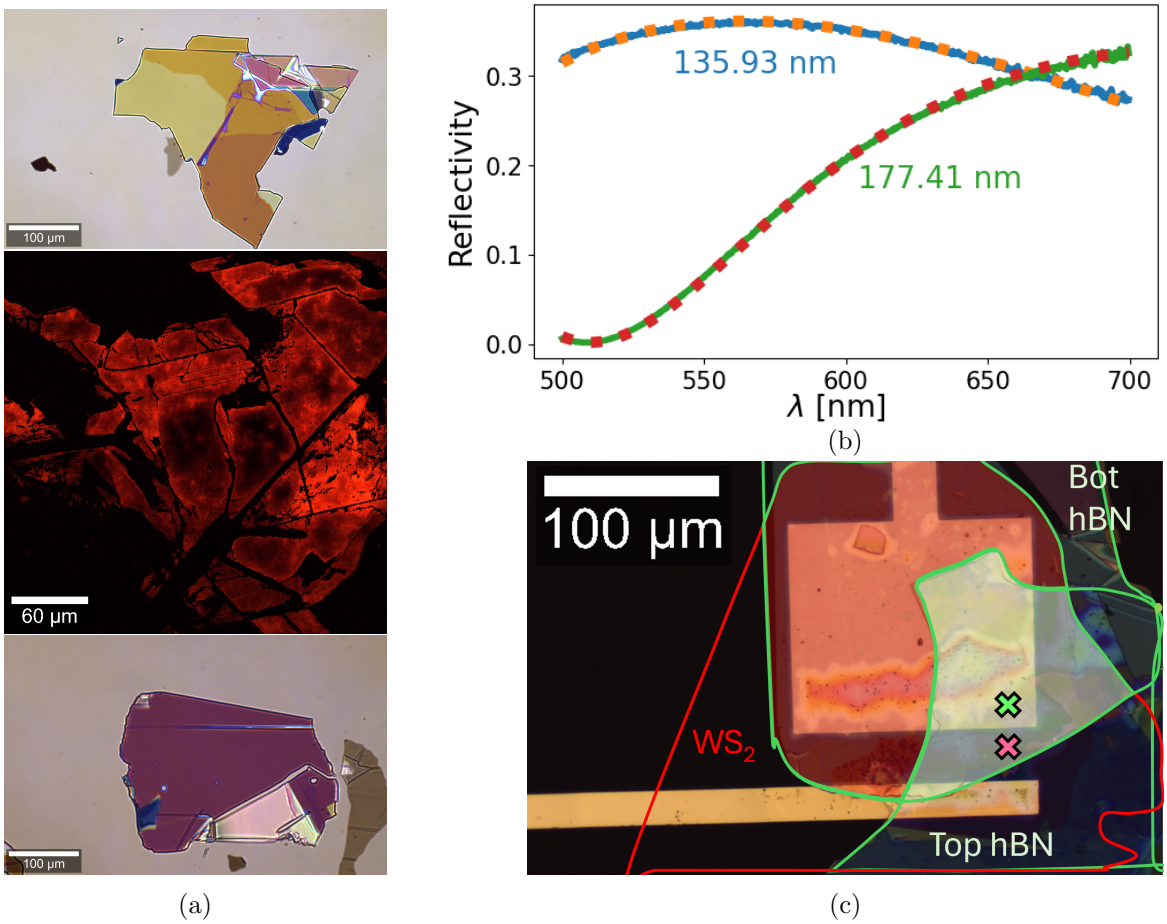

(a) (b) (c)

Figure 4.4: *(a) Materials used in the active structure,* ***(top to bottom)****: Top hBN flake, WS_2 (PL map) and bottom hBN flake. The WS_2 PL map helps determine the largest continuous section to use. (b) Measured reflectivities (solid lines) of top (blue) and bottom (green) hBN flakes with fits (dotted lines) to determine the thicknesses of each. (c) Complete structure with both hBN flakes and WS_2 on Au contacts. The positions for each laser spot while measuring phase modulation are illustrated with pink and green "X"s.*

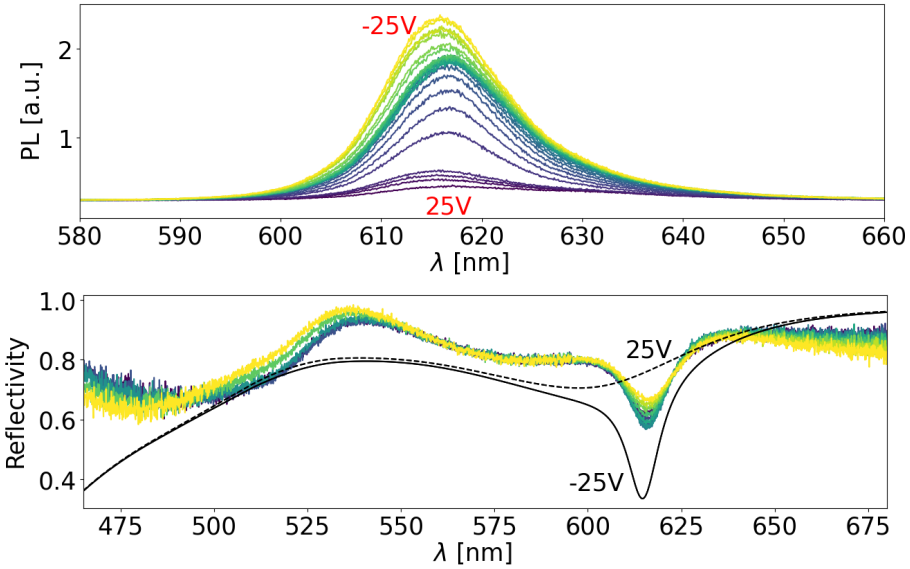

Figure 4.5: ***(top)*** *Photoluminescence (PL) and* ***(bottom)*** *reflectivity of structure in Figure 4.4 while applying various gating voltages. The exciton quenching is visible when the PL intensity drops and as reflectivity increases. The simulated reflectivity for "On" (solid-black line) and "Off" (dashed-black line) states are shown alongside the measured results.*

4.3.2 Gating Measurements

Aligning the lasers as in Figure 4.4e establishes a situation where the laser spot over the Au contact ("X") should experience a phase shift when changing the gating voltage while the other laser spot ("X") should not (assuming there is only modulation in the WS_2 excitons for areas directly above the Au contact). The results during gating can be seen in Figures 4.6 where the gating voltage is adjusted. Some clear peaks in the phase occur between sections where the gate voltage is changed. Figure 4.6a shows three different measurements stacked to demonstrate that, for each measurement, similar peaks appear after the gating voltage is changed. Figures 4.6b,c show the results from repeatedly switching between two gating voltages. While there is not a consistent phase shift during the transition periods between different voltages, there are clear peaks at several points in the process, which are shown in the plots. Figure 4.6c displays the amplitude and phase to emphasize the moment the gating voltage affects the phase.

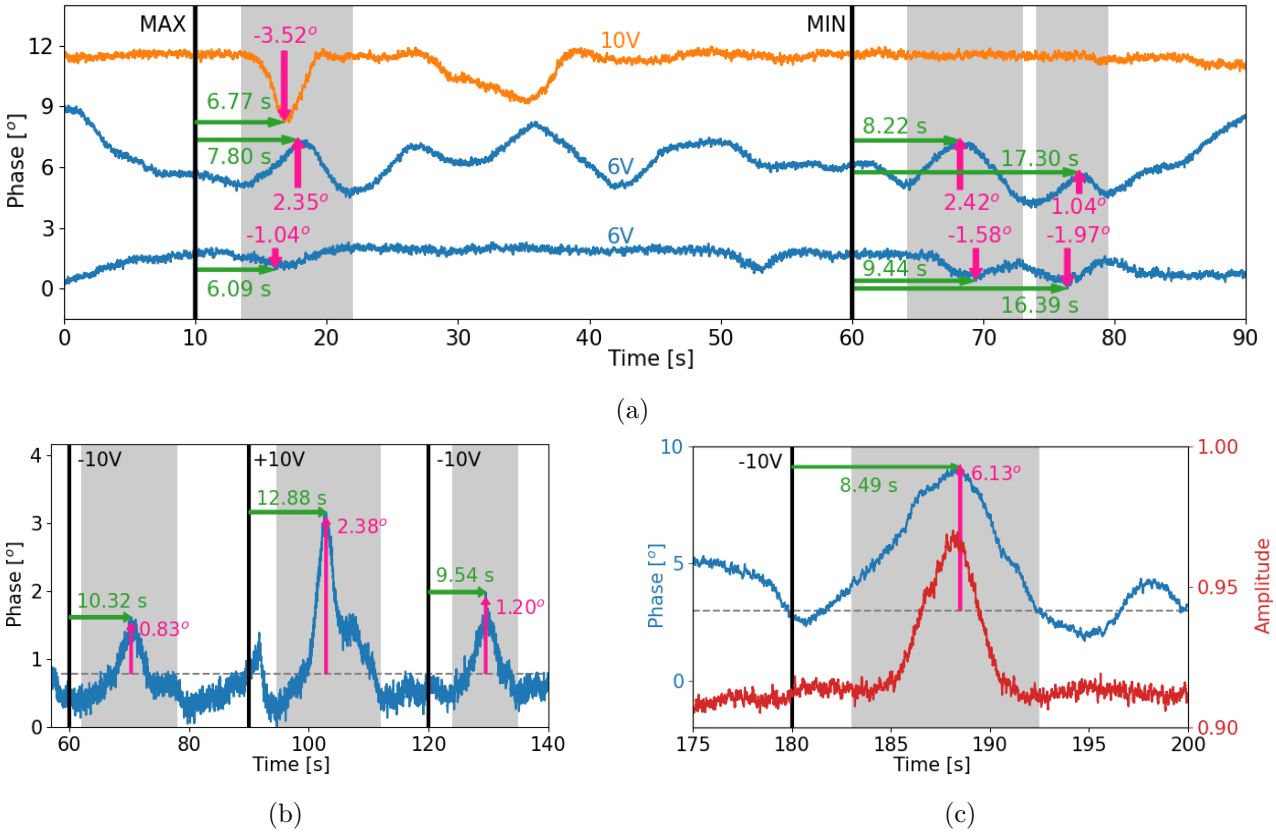

Figure 4.6: *Phase changes measured when applying a gate voltage across the structure. The phase shifts are highlighted in grey and the times when the voltage is switched is shown in black. The green and pink arrows represent the time from the previous voltage change and peak in phase compared to the average phase value, respectively. The plots show results when the voltage is varied (a) from 0 V to 6 V / 10 V to -6 V / -10 V, (b) from -10 V to 10 V repeatedly, and (c) from 10 V to 0 V repeatedly. Only a section is displayed in (b) and (c) for clarity.*

There is a consistent time delay between when the voltage is switched and measuring a phase shift for each measurement. The time delays for the peaks in Figure 4.6a agree moderately well across each dataset. Figure 4.6b,c also have consistent delays, where most peaks occur within 10 s of a voltage switch. The program adjusting voltage keeps the steps small so the voltage does not change too rapidly, thus avoiding breakdown of the material. This explains the delay between setting a new voltage and when the phase changes. Any deviations in this delay could occur from the following:

- The script running the voltage updates sometimes pauses after receiving a command. This pause could offset the exact moment the voltage begins changing.
- A physical delay by sending the command to the voltage script at slightly different times.

- The device measuring the phase sometimes skips a time step (*i.e.* the time displays 38 s $\rightarrow$ 40 s, skipping 39 s) due to an error when displaying the time during a measurement.
- Small changes in the structure between measurements or voltage changes (e.g. temperature changes) resulting in a different gradient of charge densities each time.

While each of these possibilities likely only produces a small time delay, since all peaks occur within a few seconds of a transition point, these small deviations become significant.

Comparing the experimental results to the simulations in Figure 3.8, it appears that the phase shifts are larger than expected. The phase peak varies across the datasets from $\phi < 1°$ (close to the predicted value) to $\phi \approx 6°$ (larger than expected). A possible explanation for this is thermal effects in the structure, causing movement of small defects on the surface. This would cause phase shifts even when the voltage is stable.

Any of these could explain why the results vary with a few seconds' delay between phase shifts or alter the magnitude of the phase peak. There are several possible approaches to determine the accuracy of these results to ensure they are measuring phase modulation instead of defects. These approaches are discussed further in Chapter 5.

5 Discussion and Outlook

This chapter discusses the results from Chapter 4, focusing on the differences between simulations and experiments, and provides reasons for why these differences occur. There is also a discussion on alternate measurement approaches for the active structure, which may provide interesting insight into the mechanisms behind the optical properties due to excitons. Finally, a review of the system improvements that have led to the current stability level and how they could be enhanced to further reduce susceptibility to noise and measure even smaller phase shifts.

One possible reason for the difference in the shape of the amplitude and phase plots while scanning over the sample edges in Chapter 4 could be due to the irregular beam spots. A common outcome from using AOMs is that the diffracted beams no longer resemble a clear Gaussian spot. Since the simulations always use a Gaussian spot, as in Figure 3.1, the beam spots used in these scans are expected to give a different response to the simulations. The real beam spots can be seen in Figure 5.1.

A solution to this would be to use a higher NA objective to get smaller beam spots. This would ensure that even with an imperfect beam shape, the smaller measurement area entails that any imperfections are less likely to result in significant differences between simulations and experimental results. Alternatively, the beams can be sent through a microscale (pinhole) aperture. This would produce Gaussian spots, at the expense of beam intensity [72].

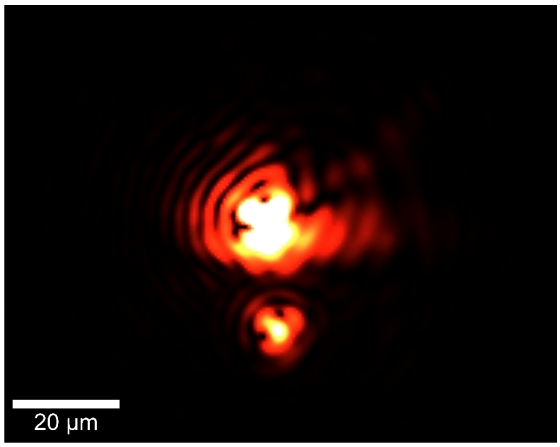

Figure 5.1: *Beam spots used for most measurements shown. Irregular shape comes from the AOMs used to frequency shift the original laser.*

Another possibility is the presence of defects (dirt, imperfect surface features, inhomogeneity within the sample) that are causing differences in the phase when scanning. As the setup is sensitive to changes of $\phi < 10^o$, defects such as residue or scratches on the surface would cause a change in the reflection phase. Also, since the laser is traveling through some samples and reflecting from the substrate, any defects within the sample material would have a similar effect on the reflection response. Finally, the measurement speed (*i.e.* the movement speed of the sample) has an impact of the results. The lock-in amplifier being used to extract the phase requires a time constant to be set to output the average of all values within this period. Larger time constants result in averaging over longer times. For all measurements in this thesis, the time constant is kept at 10 ms. This means that the movement speed must be slow enough to measure the true phase response within the period of the time constant. Decreasing this results in the phase being noisier due as small time scale fluctuations have a larger impact on the average phase output. If the phase could be stabilized further, a smaller time constant could be used to be more sensitive to very small changes in phase.

To achieve this noise reduction, a second photo-detector can be placed after the final beam-splitter in Figure 2.5 to detect the beating signal before the lasers are incident on the sample. These before and after signals should have similar noise, as they only separate at the beamsplitter. This could be used as a kind of "compensation" measurement that can be subtracted from the reflected signal to extract the pure phase response from the sample. While this is attempted during the project, the second photo-detector requires the use of a second lock-in amplifier. There is another lock-in amplifier available, and the noise is demonstrated to be the same before and after reflection, but the two devices

have different settings for time-constant, sensitivity, and for some measurements the devices didn't always produce the same output. For this reason, this method was not implemented for any of the results shown in this thesis. However, by using the same model lock-in amplifier and matching the settings, this approach shows significant potential for noise reduction.

For thinner samples (such as WS_2 and graphene), there appear to be oscillations in the amplitude and phase that only occur when the stage holding the sample is moving, and the period of the oscillation changes when the stage movement speed is changed. This indicates that the change is most likely coming from the stage itself. A possible source could be the design of the movement mechanism. The stage moves because a screw with a very small thread length rotates to pull/push the stage as it rotates. This screw could be causing a change in the height of the stage very slightly, which then causes the phase to change as the height oscillates.

Finally, the gating measurements show pretty confidently that there is phase modulation when the sample is being gated. An update to the gating voltage results in a phase shift within 10 s after the update command is sent. The timing of each peak after an update is a clear indication that there are changes in the structure that are altering the phase. These changes are also only seen in the short period after each voltage update. This further demonstrates that the phase shift is due to changes in the material, as the phase should only change when there is a $difference$ between the two laser spots (*i.e.* the spot over the Au contact is experiencing changes during modulation that the other spot is not experiencing). Once the changes in the material have settled, the phase returns to the initial value, as seen in Figure 4.6.

To further test this, measurements can be done by placing both laser spots over different positions on the structure or scanning over the structure in different directions for a range of voltages. Some examples of this are shown in Figure 5.2, where the stationary positions ("X", "X") and the scanning directions (dotted-black lines) are just some options for characterization. These measurements could provide useful information about the conditions necessary to produce modulation (e.g., how far from the Au contact does the WS_2 still experience exciton quenching). Measuring at areas without hBN on top of the WS_2 (highlighted in red) is also an option to investigate whether the hBN enhances or reduces the phase modulation for this design.

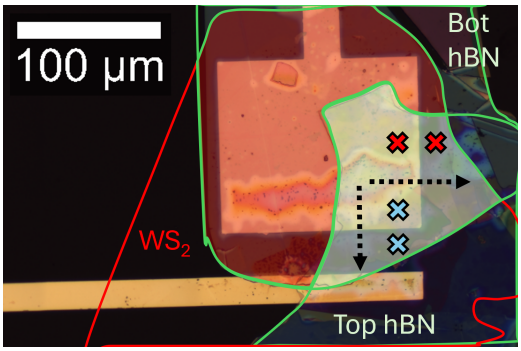

Figure 5.2: *Different laser positions to measure the phase response at different locations or while scanning in one direction compared to another. The dotted lines represent scanning directions to move the lasers across while keeping the voltage constant. The green highlighted area shows where the WS_2 is between hBN layers. The red highlighted area shows where the WS_2 is sitting on hBN without a top hBN layer.*

Another approach to characterizing this device would be to measure the phase response for smaller increments of voltage. In the examples shown in Figure 4.6, all measurements are performed by setting the voltage to a maximum or minimum and alternating between these two values (for example, 10V → -10V → 10V .....) and observing the overall phase response during this transition. However, by updating the voltage in smaller steps (*i.e.* 10V → 9V → 8V .....), the exact phase response between each interval can be observed to gain a deeper understanding of the processes occurring within the structure. These approaches could provide better insight into the mechanisms driving modulation within the monolayer structure and lead to an improvement in the design of phase modulating devices.

There are some effects present in the phase response due to movement of the stage that are not

present during the gating measurements, as the gating is static. Effects caused by variations in the stage height or defects along the surface are significant in cases where the expected phase shift is small.

All measurements were performed using incident light for $\lambda = 633$ nm and $\lambda = 532$ nm. However, neither of these lasers is at the resonance wavelength for the excitons in WS_2 (see Figure 2.11).

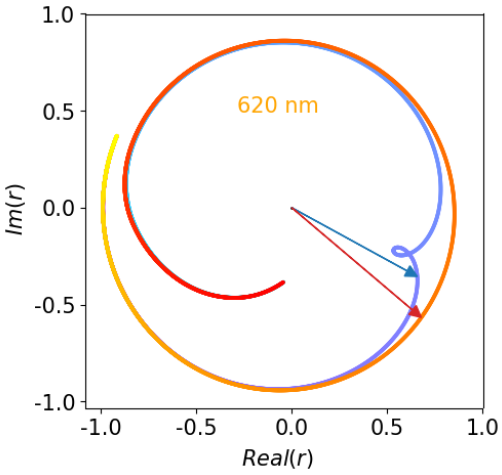

Figure 5.3: *Reflection coefficient r in the complex plane before (blue) and after (red) exciton quenching. The arrows represent the reflection phase vector for $\lambda = 620$ nm on WS_2 monolayer sandwiched between two hBN layers using the dimensions calculated in Figure 3.7.*

By probing the gated structure at a wavelength closer to the A exciton ($\lambda = 620$ nm), the phase modulation would be much greater. The expected change in the phase vector for the active structure is shown below in Figure 5.3, where the phase change is far larger than that expected or measured with the $\lambda = 532$ nm laser.

To achieve this flexibility in wavelength, a broadband tunable laser source would be coupled into the existing setup. This would provide a range of wavelengths which could be tested with just a minor amount of realignment to ensure the output from the AOM system is overlapping. There is an added consideration if the laser source is a pulsed system instead of a broadband CW laser.

One of the benefits of using a laser source that has power modulation is the decreased susceptibility to noise in the system. Each iteration leading to the SDHM setup had the main goal of optimizing the optical setup to improve the phase stability in the presence of unavoidable noise, since the 633 nm HeNe laser did not have power modulation. However, the 532 nm laser is capable of increasing laser power, thus improving the phase stability by increasing the signal-to-noise ratio. This is clear in Figure 5.4, where the stability is compared to each iteration (as in Figure 2.9) with the increased laser power clearly showing a reduced drift.

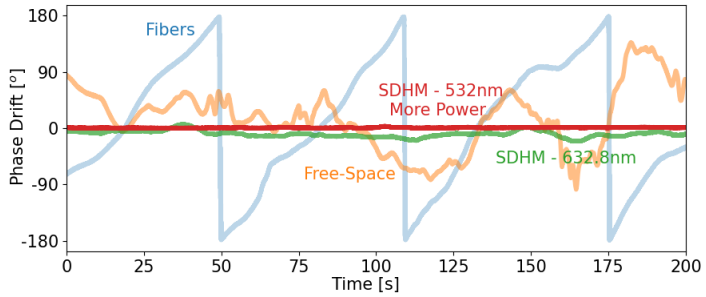

Figure 5.4: *Phase shift for each iteration of the setup, including the stability for the SDHM setup with two different wavelengths.*

Setup	Phase Drift	
	[°/min]	[nm/min]
Fibers	284.99	501.10
Free-Space	4.65	8.17
SDHM - 633 nm	1.48	2.61
SDHM - 532 nm	0.08	0.12

Table 5.1: *Phase drift for each setup, now with the SDHM setup using more power (red) at $\lambda = 532$ nm.*

Comparing the values in Table 5.1, the drift is approximately 20 times lower for the SDHM setup with power modulation, and can likely go lower if the power is increased further. This indicates that increasing laser power is one solution to improve phase stability and have much clearer results for measurements that are more challenging (for example, low reflectivity samples or small expected phase shifts).

6 Conclusion

In this thesis, we have explored how scanning differential heterodyne microscopy can be used to measure amplitude and phase changes for a 2D material in an active structure. By observing the change in reflection phase while applying a gate voltage, we demonstrated that the phase upon reflection from this structure changes when the charge carrier density is controlled.

This has been achieved by first determining the conditions necessary to measure the phase of visible light in Chapter 2. By implementing this approach experimentally, we've shown that the phase and amplitude can be simultaneously measured. Furthermore, by improving the stability of the phase through several iterations of the system, the phase drift can be reduced to as low as $\phi = 0.08°$ per minute.

After the setup has been improved, Chapter 3 explains the theory behind the transfer matrix method and its application in determining the reflected responses from various samples. The theoretical model developed in this chapter is validated using previous literature that applies the same technique. The model, once validated, is used to determine the design of an active structure that incorporates a 2D material intended to be electrically gated. The structure design is optimized to produce the largest phase change whilst modifying the gate voltage.

Finally, Chapter 4 describes the approach taken to benchmark the system, which determines that the smallest phase shift measurable with a moving sample is as low as $\phi = 2°$. Various samples are tested to determine the functionality of the system under different conditions (transparent versus non-transparent substrate) and varied sample heights, all of which have good agreement with simulated results. The fabrication of the active structure is shown, along with an analysis of the device's optical properties (photoluminescence, reflectivity) during electrical gating. The outcome from this analysis shows that the gate voltage alters the optical properties and confirms the strong exciton resonance within the structure. The chapter concludes with Section 4.3.2, where the reflection phase of the structure is observed while changing the gate voltage. These measurements show a clear change in the phase response whenever the voltage is adjusted, supporting the model's predictions that adjusting the exciton resonance within the structure induces a change in the phase response.

This thesis demonstrates the ability to accurately measure the phase response in the visible spectrum from an active structure that exploits the optical properties of 2D materials. Such measurements are crucial for the development of more compact, cheaper, and electrically tunable optical devices.

To improve upon the results shown in this thesis, further work on the active structure should be performed to fully understand the mechanisms driving the phase modulation. Measurements at different wavelengths, using different materials/ structure designs, and including additional noise-reducing techniques, would lead to a deeper understanding of the operation of these devices, thus promoting their development in the future.

7 Acknowledgments

This year has been full of support and encouragement from a lot of people whom I would like to express my deepest thanks to.

Firstly, I'd like to thank **Jorik van de Groep** for the opportunity to work in the group. This project has been a lot of fun and opened my eyes to the joy of experimental research. Also, thank you for the continuous support and feedback throughout the year to keep me improving. I've truly learned so much during the year, so I'm incredibly grateful for this opportunity.

Secondly, I would like to thank my supervisors, **Bernardo S. Dias** and **Tom Hoekstra**. The support you offered throughout the year was crucial in helping me reach the goals achieved in this thesis. Your continuous aid with technical problems, simulation errors, and all-encompassing physics questions is what got me to the final results.

Thirdly, I would like to thank **Gaby Mentasti**, **Mehmet Atıf Durmuş**, **Eva Almeida**, **Freek van Gorp**, **Bauke van der Vorm**, **Thomas Bauer**, **Reynolds Dziobek Garrett**, **Sander Mann**, and **Charly Bolhuis**. The atmosphere at the lunch table was never dull, and I thoroughly enjoyed working with every one of you, no matter what capacity it was. Whether you helped me with thesis work, gave me advice on some problem, or just had lunch and a coffee with me, every little thing was important to me and made my time during the year a joy. The team and everyone associated with it have been an absolute pleasure.

Finally, I'd like to thank **Louis**, **Max**, **Suus**, **Aditi**, **Neda**, **Halid**, **Luna**, **Alicja**, **Natalia**, **Marein**, **Ben**, and **AMEP Class 2025**. While I never got to work directly with you for my project, the support you provided me outside of my project was essential to me. The random hangouts, watching shows and movies, sitting in the sun, and going on trips were often hilarious and unforgettable. The memories I've made during the master's are some of my favorites and will be cherished, along with all those we still have to make.

My apologies to anyone who has been missed in this. There have been so many important people to me during these last two years, and I hope that, even if your name isn't included above, you know you're included in my gratitude.

Bibliography

[1] Timothy C Kriss and Vesna Martich Kriss. History of the operating microscope: from magnifying glass to microneurosurgery. *Neurosurgery*, 42(4):899–907, 1998.

[2] Kostya S Novoselov, Da Jiang, F Schedin, TJ Booth, VV Khotkevich, SV Morozov, and Andre K Geim. Two-dimensional atomic crystals. *Proceedings of the National Academy of Sciences*, 102 (30):10451–10453, 2005.

[3] Hou-Tong Chen, Antoinette J Taylor, and Nanfang Yu. A review of metasurfaces: physics and applications. *Reports on progress in physics*, 79(7):076401, 2016.

[4] Aobo Li, Shreya Singh, and Dan Sievenpiper. Metasurfaces and their applications. *Nanophotonics*, 7(6):989–1011, 2018.

[5] Ludovica Guarneri, Qitong Li, Thomas Bauer, Jung-Hwan Song, Ashley P Saunders, Fang Liu, Mark L Brongersma, and Jorik van de Groep. Temperature-dependent excitonic light manipulation with atomically thin optical elements. *Nano Letters*, 24(21):6240–6246, 2024.

[6] Luis A Jauregui, Andrew Y Joe, Kateryna Pistunova, Dominik S Wild, Alexander A High, You Zhou, Giovanni Scuri, Kristiaan De Greve, Andrey Sushko, Che-Hang Yu, et al. Electrical control of interlayer exciton dynamics in atomically thin heterostructures. *Science*, 366(6467):870–875, 2019.

[7] Qiaoliang Bao, Han Zhang, Bing Wang, Zhenhua Ni, Candy Haley Yi Xuan Lim, Yu Wang, Ding Yuan Tang, and Kian Ping Loh. Broadband graphene polarizer. *Nature photonics*, 5(7): 411–415, 2011.

[8] Nathan Youngblood, Yoska Anugrah, Rui Ma, Steven J Koester, and Mo Li. Multifunctional graphene optical modulator and photodetector integrated on silicon waveguides. *Nano letters*, 14 (5):2741–2746, 2014.

[9] Jin Tae Kim, Kwang Hyo Chung, and Choon-Gi Choi. Thermo-optic mode extinction modulator based on graphene plasmonic waveguide. *Optics express*, 21(13):15280–15286, 2013.

[10] Zhipei Sun, Amos Martinez, and Feng Wang. Optical modulators with 2d layered materials. *Nature Photonics*, 10(4):227–238, 2016.

[11] Bernardo S Dias and Jorik van de Groep. High-na 2d image edge detection using tamm plasmon polaritons in few-layer stratified media. *ACS Photonics*, 12(1):311–319, 2024.

[12] Giada R La Gala, Arvind S Kumar, Rick Leijssen, Ewold Verhagen, and Juha T Muhonen. Quadrature-averaged homodyne detection for cavity parameter estimation. *arXiv preprint arXiv:2209.05807*, 2022.

[13] Hedi Bellil and Mustafa AG Abushagur. Heterodyne detection for fiber bragg grating sensors. *Optics & Laser Technology*, 32(5):297–300, 2000.

[14] NDT Resource Center. Impedance. https://www.nde-ed.org/Physics/Waves/Impedance.xhtml, 2023. URL https://www.nde-ed.org/Physics/Waves/Impedance.xhtml.

[15] John H Scofield. Frequency-domain description of a lock-in amplifier. *American journal of physics*, 62(2):129–132, 1994.

[16] Daniel J McCarron. A guide to acousto-optic modulators. *: http://massey. dur. ac. uk/resources/slcornish/AOMGuide. pdf*, 2007.

[17] Christopher Palmer and Erwin G Loewen. Diffraction grating handbook. 2005.

[18] Eugene I Gordon. A review of acoustooptical deflection and modulation devices. *Applied optics*, 5(10):1629–1639, 1966.

[19] AA Opto-electronic. Mt200-a0.5-vis acousto-optic tunable filter. Product page / specification sheet, 2024. URL https://aaoptoelectronic.com/mt200-a0-5-vis/.

[20] AA Opto-electronic. Mpds(e)ncmx multi-output multichannel digital synthesizers, external clock. Product page / specification sheet, 2025. URL https://aaoptoelectronic.com/mpdsencmx-multi-ouput-multi-channel-digital-synthesizers/.

[21] AA Opto-electronic. *MPDSnCmX / MPDSEPnCmX Multi-output Multichannel Digital Synthesizers Datasheet (HR-d024)*. AA Opto-electronic, March 2024. URL https://aaoptoelectronic.com/wp-content/uploads/2024/03/MPDSnCmX-MPDSEPnCmX-HR-d024.pdf.

[22] Melles Griot. *05-LHP Helium Neon Laser Datasheet (05-LHP-211/151/991)*. Artisan Technology Group (as hosted by ArtisantG), 2019. URL https://www.artisantg.com/info/Melles_Griot_05_LHP_Datasheet_2019731111233.pdf.

[23] IM Akhmedzhanov, DV Baranov, and Evgeny M Zolotov. Object characterization with a differential heterodyne microscope. *Journal of optics A: Pure and applied optics*, 5(5):S200, 2003.

[24] Nikon Instruments Inc. Objective comparison — objective selector. Website, 2025. URL https://www.microscope.healthcare.nikon.com/products/optics/selector/comparison/-1824.

[25] Thorlabs, Inc. Pda100a2 – si switchable gain detector, 320–1100 nm, 11 mhz bandwidth. Product page, 2018. URL https://www.thorlabs.com/thorproduct.cfm?partnumber=PDA100A2. Release Date: March 1 2018.

[26] Stanford Research Systems (ThinkSRS). Sr830 dsp lock-in amplifier. Product page / specification sheet, 2025. URL https://www.thinksrs.com/products/sr830.html.

[27] IM Akhmedzhanov, DV Baranov, and EM Zolotov. Investigation of diffraction gratings with the use of a differential heterodyne microscope. *Optics and spectroscopy*, 96:635–640, 2004.

[28] Nick J Schilder, Tom AW Wolterink, Christiaan Mennes, Ruslan Röhrich, and A Femius Koenderink. Phase-retrieval fourier microscopy of partially temporally coherent nanoantenna radiation patterns. *Optics Express*, 28(25):37844–37859, 2020.

[29] Adarsh B Vasista, Deepak K Sharma, and GV Kumar. Fourier plane optical microscopy and spectroscopy. *arXiv preprint arXiv:1806.08280*, 2018.

[30] Arne M. Sikkink. Back focal plane of microscope objectives. https://amsikking.github.io/microscope_objectives/back_focal_plane.html, 2020.

[31] Wikipedia contributors. Objective (optics) — wikipedia, the free encyclopedia. https://en.wikipedia.org/wiki/Objective_%28optics%29, 2025.

[32] Lumen Learning. Young's double slit experiment. *Fundamentals of Heat, Light & Sound*, 2021.

[33] Michele Buscema, Joshua O Island, Dirk J Groenendijk, Sofya I Blanter, Gary A Steele, Herre SJ van der Zant, and Andres Castellanos-Gomez. Photocurrent generation with two-dimensional van der waals semiconductors. *Chemical Society Reviews*, 44(11):3691–3718, 2015.

[34] I Cheliotis and I Zergioti. A review on transfer methods of two-dimensional materials. *2D Materials*, 11(2):022004, 2024.

[35] Andre K Geim. Graphene prehistory. *Physica Scripta*, 2012(T146):014003, 2012.

[36] Darshana Wickramaratne, Leigh Weston, and Chris G Van de Walle. Monolayer to bulk properties of hexagonal boron nitride. *The Journal of Physical Chemistry C*, 122(44):25524–25529, 2018.

[37] Jiapeng Liu, Huibin Liu, Wenchao Peng, Yang Li, Fengbao Zhang, and Xiaobin Fan. High-yield exfoliation of mos2 (ws2) monolayers towards efficient photocatalytic hydrogen evolution. *Chemical Engineering Journal*, 431:133286, 2022.

[38] Nicolas Mounet, Marco Gibertini, Philippe Schwaller, Davide Campi, Andrius Merkys, Antimo Marrazzo, Thibault Sohier, Ivano Eligio Castelli, Andrea Cepellotti, Giovanni Pizzi, et al. Two-dimensional materials from high-throughput computational exfoliation of experimentally known compounds. *Nature nanotechnology*, 13(3):246–252, 2018.

[39] Sajedeh Manzeli, Dmitry Ovchinnikov, Diego Pasquier, Oleg V Yazyev, and Andras Kis. 2d transition metal dichalcogenides. *Nature Reviews Materials*, 2(8):1–15, 2017.

[40] Kin Fai Mak, Changgu Lee, James Hone, Jie Shan, and Tony F Heinz. Atomically thin mos 2: a new direct-gap semiconductor. *Physical review letters*, 105(13):136805, 2010.

[41] Andrea Splendiani, Liang Sun, Yuanbo Zhang, Tianshu Li, Jonghwan Kim, Chi-Yung Chim, Giulia Galli, and Feng Wang. Emerging photoluminescence in monolayer mos2. *Nano letters*, 10 (4):1271–1275, 2010.

[42] Simon M Sze, Yiming Li, and Kwok K Ng. *Physics of semiconductor devices*. John wiley & sons, 2021.

[43] CODATA Committee. 2018 codata value: Planck constant. https://physics.nist.gov/cgi-bin/cuu/Value?h, 2019.

[44] CODATA Committee. 2018 codata value: Speed of light in vacuum. https://physics.nist.gov/cgi-bin/cuu/Value?c, 2019.

[45] Alexey Chernikov, Timothy C Berkelbach, Heather M Hill, Albert Rigosi, Yilei Li, Burak Aslan, David R Reichman, Mark S Hybertsen, and Tony F Heinz. Exciton binding energy and nonhydrogenic rydberg series in monolayer ws 2. *Physical review letters*, 113(7):076802, 2014.

[46] Mark Fox. *Optical properties of solids*, volume 3. Oxford university press, 2010.

[47] D. E. Aspnes and A. A. Studna. Refractive index of si (silicon) — data compiled by aspnes studna. RefractiveIndex.INFO database, 2025. URL https://www.refractiveindex.info/?shelf=main&book=Si&page=Aspnes. Accessed: 2025-07-13; data originally published in Phys. Rev. B 27, 985–1009 (1983).

[48] Brian T Schwartz and Rafael Piestun. Total external reflection from metamaterials with ultralow refractive index. *Journal of the Optical Society of America B*, 20(12):2448–2453, 2003.

[49] JG Gay. Screening of excitons in semiconductors. *Physical Review B*, 4(8):2567, 1971.

[50] Yilei Li, Alexey Chernikov, Xian Zhang, Albert Rigosi, Heather M Hill, Arend M Van Der Zande, Daniel A Chenet, En-Min Shih, James Hone, and Tony F Heinz. Measurement of the optical dielectric function of monolayer transition-metal dichalcogenides: Mos 2, mose2, ws 2, and wse2. *Physical Review B*, 90(20):205422, 2014.

[51] Yilei Li, Alexey Chernikov, Xian Zhang, Albert Rigosi, Heather M Hill, Arend M Van Der Zande, Daniel A Chenet, En-Min Shih, James Hone, and Tony F Heinz. Measurement of the optical dielectric function of monolayer transition-metal dichalcogenides: Mos 2, mo s e 2, ws 2, and ws e 2. *Physical Review B*, 90(20):205422, 2014.

[52] Anthony Gerrard and James M Burch. *Introduction to matrix methods in optics*. Courier Corporation, 1994.

[53] Betty Isabelle Bleaney and Brebis Bleaney. *Electricity and Magnetism, Volume 2*, volume 1. Oxford University Press, USA, 2013.

[54] Zahraa Hummam Mohammed. The fresnel coefficient of thin film multilayer using transfer matrix method tmm. In *IOP Conference Series: Materials Science and Engineering*, volume 518, page 032026. IOP Publishing, 2019.

[55] Kiyoshi Yamamoto and Hatsuo Ishida. Interpretation of reflection and transmission spectra for thin films: reflection. *Applied Spectroscopy*, 48(7):775–787, 1994.

[56] RP Photonics Consulting GmbH. Polarization of light – definition, types, and applications. https://www.rp-photonics.com/polarization_of_light.html, 2025.

[57] Bernd Harbecke. Coherent and incoherent reflection and transmission of multilayer structures. *Applied Physics B*, 39:165–170, 1986.

[58] Peter Markos and Costas M Soukoulis. Wave propagation: from electrons to photonic crystals and left-handed materials. In *Wave Propagation*. Princeton University Press, 2008.

[59] Tom G Mackay and Akhlesh Lakhtakia. *The transfer-matrix method in electromagnetics and optics*. Springer Nature, 2022.

[60] Steven J. Byrnes. tmm: Transfer matrix method for multilayer thin films. PyPI Package, 2024. URL https://pypi.org/project/tmm/. Accessed: 2025-07-13; Documentation available at https://github.com/sbyrnes321/tmm.

[61] Steven J Byrnes. Multilayer optical calculations. *arXiv preprint arXiv:1603.02720*, 2016.

[62] Amnon Yariv and Pochi Yeh. Optical waves in crystal propagation and control of laser radiation. 1983.

[63] IM Akhmedzhanov and SI Bozhevolnyi. Scanning differential microscopy for characterization of reflecting phase-gradient metasurfaces. *Optics Communications*, 427:603–608, 2018.

[64] Ildar M Akhmedzhanov, Rucha A Deshpande, Dmitry V Baranov, and Sergey I Bozhevolnyi. Characterization of gap-plasmon based metasurfaces using scanning differential heterodyne microscopy. *Scientific Reports*, 10(1):13524, 2020.

[65] Itai Epstein, Bernat Terrés, André J Chaves, Varun-Varma Pusapati, Daniel A Rhodes, Bettina Frank, Valentin Zimmermann, Ying Qin, Kenji Watanabe, Takashi Taniguchi, et al. Near-unity light absorption in a monolayer ws2 van der waals heterostructure cavity. *Nano letters*, 20(5): 3545–3552, 2020.

[66] Ho Seung Lee, Junghyun Sung, Dong-Jin Shin, and Su-Hyun Gong. The impact of hbn layers on guided exciton-polariton modes in ws2 multilayers. *Nanophotonics*, 13(8):1475–1482, 2024.

[67] Emilio Pisanty. Phase shift for reflection and transmission on absorptive medium with complex refractive index. https://physics.stackexchange.com/q/442355, 2018. Physics Stack Exchange.

[68] Atte Haapalinna, Petri Kärhä, and Erkki Ikonen. Spectral reflectance of silicon photodiodes. *Applied optics*, 37(4):729–732, 1998.

[69] Anis Ben Slimane and Azza Ouled Zaid. Real-time fast fourier transform-based notch filter for single-frequency noise cancellation: Application to electrocardiogram signal denoising. *Journal of Medical Signals & Sensors*, 11(1):52–61, 2021.

[70] Andrea Splendiani, Liang Sun, Yuanbo Zhang, Tianshu Li, Jonghwan Kim, Chi-Yung Chim, Giulia Galli, and Feng Wang. Emerging photoluminescence in monolayer mos2. *Nano letters*, 10 (4):1271–1275, 2010.

[71] AR Cadore, BLT Rosa, I Paradisanos, S Mignuzzi, D De Fazio, EM Alexeev, A Dagkli, JE Muench, G Kakavelakis, SM Shinde, et al. Monolayer ws2 electro-and photo-luminescence enhancement by tfsi treatment. *2D Materials*, 11(2):025017, 2024.

[72] Edmund Optics. Understanding spatial filters. https://www.edmundoptics.eu/knowledge-center/application-notes/lasers/understanding-spatial-filters, n.d. Accessed: 2025-07-17.

[73] NKT Photonics. Nkt superk extreme high power supercontinuum laser, . URL https://www.gophotonics.com/products/lasers/nkt-photonics/29-650-superk-extreme.

[74] NKT Photonics. Nkt superk select tunable multi-channel filter, . URL https://www.nktphotonics.com/products/supercontinuum-white-light-lasers/superk-select/.

A Supplementary Material

This appendix goes into details for some aspects of the thesis that don't seem appropriate for the main content. The first section shows the setup designs, now accompanied with photos to show the implementation. Then the characterization of the AOM box for a range of wavelengths in the visible spectrum to determine the feasibility of using different wavelengths. Finally, the simulations for the SDHM setup are performed again, but this time for a single incident beam, instead of two incident beams as in the SDHM system.

A.1 Setup Designs with Photos

This section shows photos of each setup described previously to show how each design is implemented. The evolution of each can be seen clearly, from fibers to free space to SDHM, with the final being the design used for all measurements. The first is the fiber setup in Figure A.1. The images show the inside of the AOM box, highlighting the AOMs (blue), and the other beam path inside the yellow fiber. Following this, Figure A.2 shows the changes made to incorporate more free space components, intending to reduce phase noise. Finally, Figure A.3 shows the final setup design used for every measurement shown in this thesis.

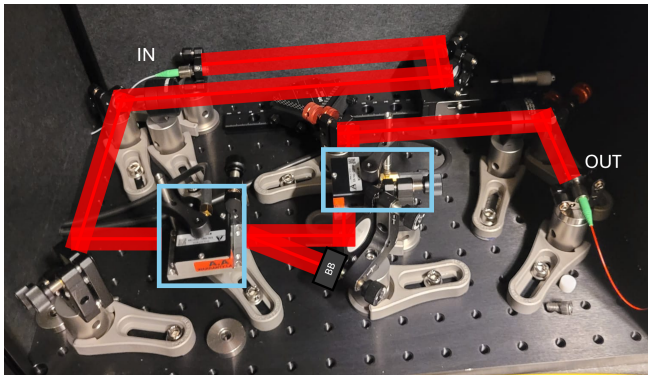

(a)

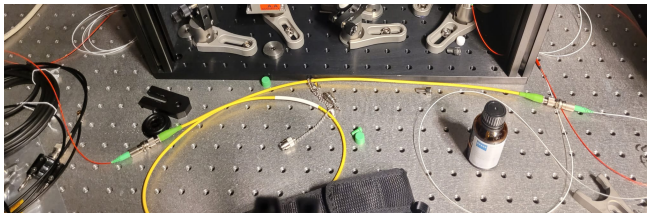

(b)

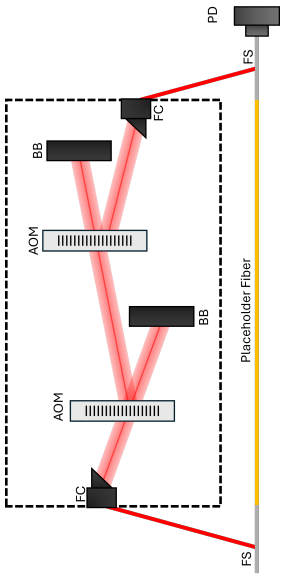

(c)

Figure A.1: (a) Optical setup for the laser path that goes through two AOMs. The first AOM downshifts the frequency of the laser by 200.020 kHz, and the second AOM upshifts the laser frequency by 199.980 kHz. (b) The yellow fiber in front of the AOM box is the second path, which is intended to go to a sample for reflection measurements. The AOM box for the first path is positioned behind the yellow fiber. Left of the AOM box are two visible fibers (red and white), which belong to the fiber-optic coupler coming from the laser that splits the laser into two separate paths. A fiber splitter recombining the beams before hitting the photo-detector is seen to the right of the AOM box. (c) Schematic for the setup in images (a)(b).

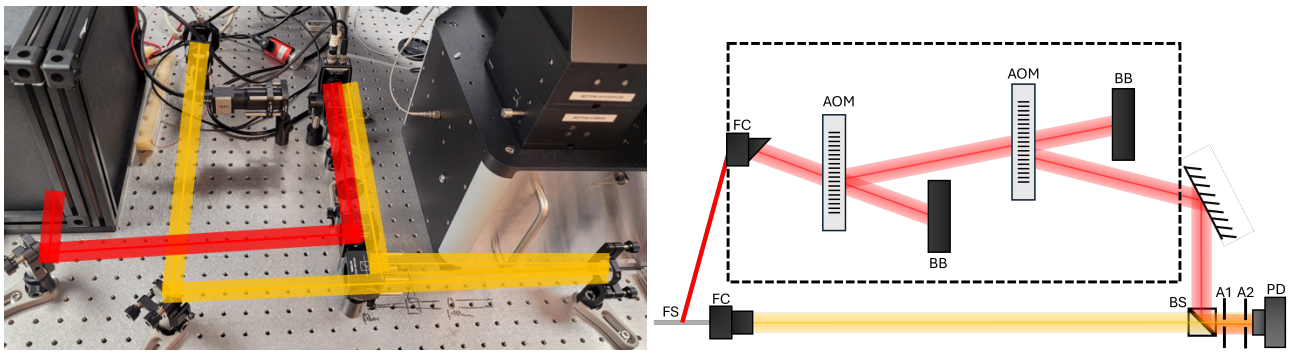

Figure A.2: (a) Free-space setup that is replacing the fibers in Figure A.1. To test the setup, the mirror in front of the microscope **(right)** is oriented to reflect the light straight back to the beam-splitter. However, when the beam is being used for sample measurements, it will be oriented so the laser goes into the bottom of the microscope. (b) Schematic of the free space setup, showing the output of the AOM box (red) and the yellow fiber now in free space.

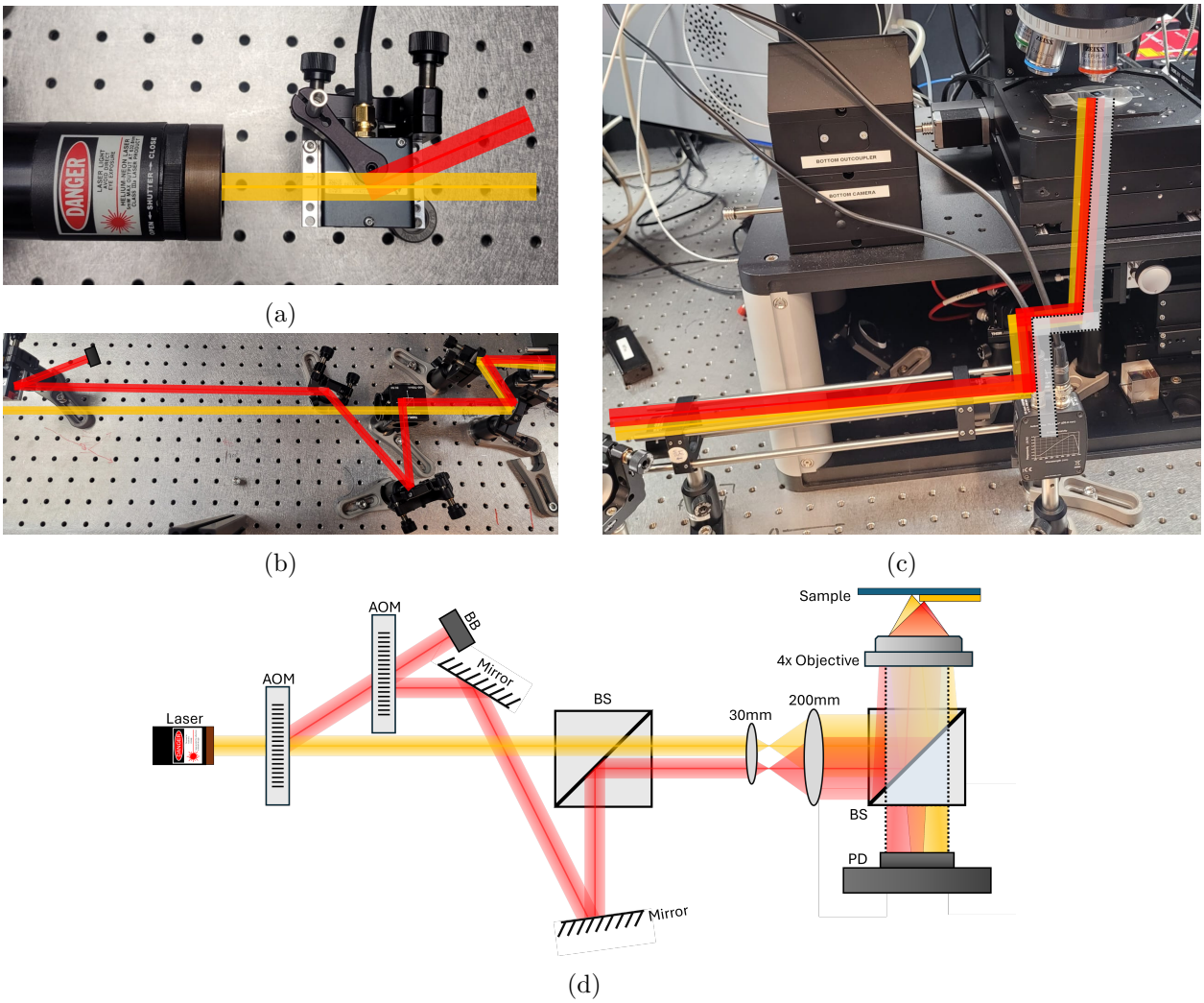

Figure A.3: Implementing a common path scheme to further reduce noise in phase measurements. Laser path follows (a) → (c). The reflected light's path is shown in white in (c). (d) Schematic of setup shown in (a)-(c).

A.2 AOM Characterization - Different Wavelengths

The components in the AOM box in Figure 2.5 are aligned for the HeNe 632.8 nm laser. However, it is useful to know what other wavelengths can be used without having to realign any components. The CW HeNe laser source is replaced with an NKT SuperK Extreme supercontinuum laser that has a supercontinuum laser source to determine the bandwidth of the system in the visible regime [73] [74]. Since the AOMs act as a diffraction grating, the $\pm 1^{st}$ order beams will diffract with different angles depending on the wavelength of light. The diffraction angle θ is related to the wavelength λ based on Equation 2.5, where now d is the distance between adjacent gratings in the diffraction grating [17]. Equation 2.5 is used here as each grating is a slit as in Figure 2.8.

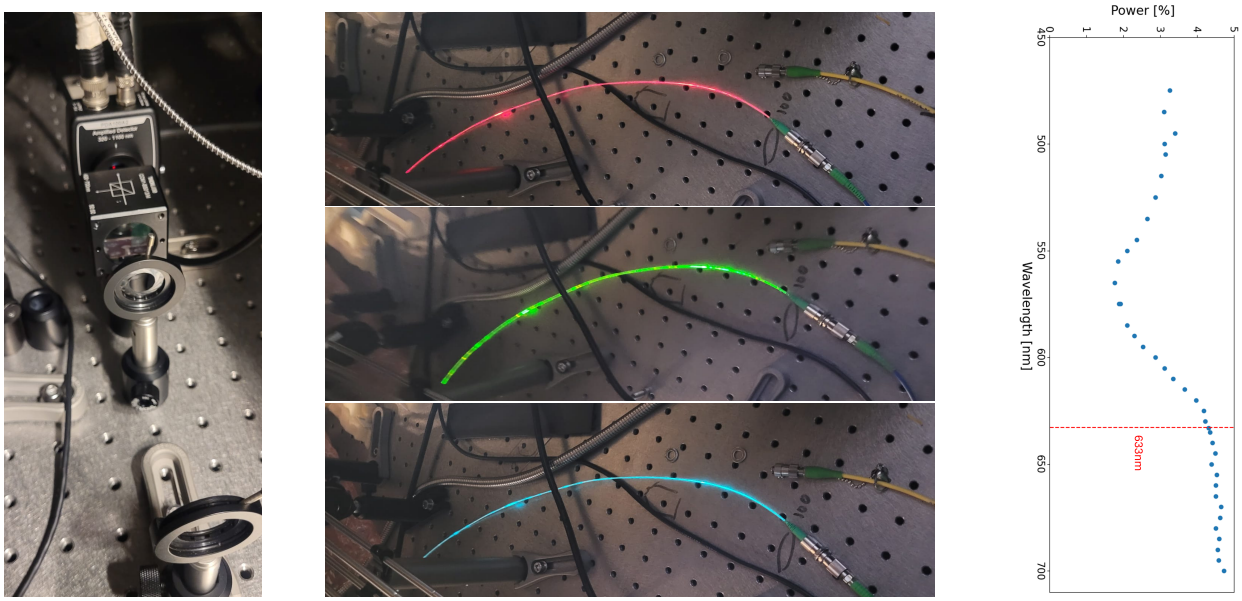

(a) (b) (c)

Figure A.4: *Replacing the HeNe laser with the NKT SuperK laser. (a) Powermeter placed to measure power of light that reaches the detector. (b) Different wavelengths of light being sent to the AOM box through the fiber. (c) Percentage of power (relative to power entering AOM box) that reaches the detector for various wavelengths. The HeNe 633 nm laser is shown as a red dotted line.*

By replacing a power meter at the detector, the relative power output of the AOM box can be characterized for visible wavelengths. Figure A.4 shows that while the setup is aligned for a 632.8 nm laser there is the possibility to use other wavelengths without adjusting any components ($\lambda > 633$ nm have similar power outputs). The drop in power for $\lambda < 633$ nm occurs when the first order spot is replaced by a higher order due to the diffraction angle decreasing for lower wavelengths in Equation 2.5. Practically, the setup will need realignment for each wavelength to ensure maximum output from the AOMs and sufficient overlap of the beams. For most of the measurements in this thesis only $\lambda = 633$ nm is used.

A.3 Simulations - Single Incident Beam

As the setup used for all experiments employs two incident beams, only simulations involving two beams are performed. However, the initial setup design utilizes just one incident beam, while keeping the other away from the sample as a reference. The simulations for the situation with only one incident beam are shown below.

Following from Equation 2.4, the expected changes in the interference signal when moving from

one material to another can be written as:

$$\begin{aligned} r_1 = |r_1|e^{i\phi_1} \qquad r_2 = |r_2|e^{i\phi_2} \\ I_{\text{Beat},1} \propto |r_1|AB\cos\left(\Delta\omega.t + \phi_1\right) \\ I_{\text{Beat},2} \propto |r_2|AB\cos\left(\Delta\omega.t + \phi_2\right) \end{aligned} \tag{A.1}$$

Equations A.1 describe the two scenarios that can occur, either the incident beam is on material 1 or material 2. When scanning across the border between the materials, the change in amplitude and phase is expected to transition from one scenario to the other, as seen in Figure A.5 (in this case, the material is the same but there is an increase in height at $x = 12.5$ μm). The steepness of the transitions are determined by the beam spot size, where higher NA (and therefore smaller spot size) leads to a sharper phase and amplitude change. There is a distinct difference in Equations A.1, where the amplitude is dependent on $|r_n|$ instead of $|r_n|^2$ as in 3.2, and there is only one transition in amplitude and phase, while with two incident beams there are two transitions. This can also be seen in Figure A.5.

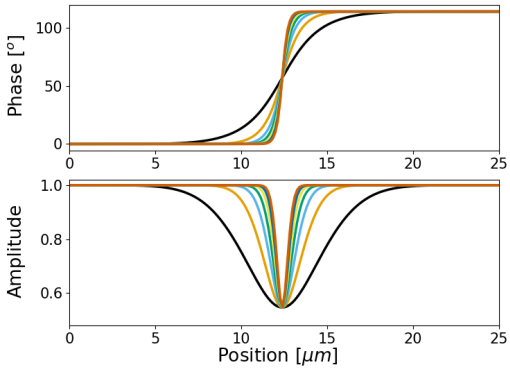

Figure A.5: *Phase **(top)** and amplitude **(bottom)** responses with a single incident beam scanning over an interface.*

The changes in amplitude and phase can be calculated using the same approach as before. Now, the change in amplitude across the interface is:

$$\Delta I_{\text{Beat}} = \frac{I_{\text{Beat},1}}{I_{\text{Beat},2}} = \frac{|AB||r_1|}{|AB||r_2|} = \frac{|r_1|}{|r_2|}. \tag{A.2}$$

So, the change in amplitude of the beating signal when going from one material to another is equal to the ratio of the reflection coefficients for each material.

The phase change will always be equal to the difference in phase pickup between each surface, and is given by:

$$\Delta\phi = \phi_1 - \phi_2 \tag{A.3}$$